

The Substructure Hierarchy in Dark Matter Haloes

Carlo Giocoli¹ *, Giuseppe Tormen², Ravi K. Sheth³, Frank C. van den Bosch⁴

¹*Zentrum für Astronomie, ITA, Universität Heidelberg, Albert-Ueberle-Str. 2, 69120 Heidelberg, Germany*

²*Dipartimento di Astronomia, Università degli Studi di Padova, Vicolo dell'osservatorio 2 I-35122 Padova, Italy*

³*Center for Particle Cosmology, University of Pennsylvania, 209 S. 33rd Street Philadelphia, PA 19104-6396*

⁴*Department of Physics & Astronomy, University of Utah, 115 South 1400 East, Salt Lake City, UT 84112-0830*

ABSTRACT

We present a new algorithm for identifying the substructure within simulated dark matter haloes. The method is an extension of that proposed by Tormen et al. (2004) and Giocoli et al. (2008a), which identifies a subhalo as a group of self-bound particles that prior to being accreted by the *main* progenitor of the host halo belonged to one and the same progenitor halo (hereafter ‘satellite’). However, this definition does not account for the fact that these satellite haloes themselves may also have substructure, which thus gives rise to sub-subhaloes, etc. Our new algorithm identifies substructures at all levels of this hierarchy, and we use it to determine the mass function of all substructure (counting sub-haloes, sub-subhaloes, etc.). On average, haloes which formed more recently tend to have a larger mass fraction in substructure and to be less concentrated than average haloes of the same mass. We provide quantitative fits to these correlations. Even though our algorithm is very different from that of Gao et al. (2004), we too find that the subhalo mass function per unit mass at redshift $z = 0$ is universal. This universality extends to any redshift only if one accounts for the fact that host haloes of a given mass are less concentrated at higher redshifts, and concentration and substructure abundance are anti-correlated. This universality allows a simple parametrization of the subhalo mass function integrated over all host halo masses, at any given time. We provide analytic fits to this function which should be useful in halo model analyses which equate galaxies with halo substructure when interpreting clustering in large sky surveys. Finally, we discuss systematic differences in the subhalo mass function that arise from different definitions of (host) halo mass.

Key words: galaxies: halo - cosmology: theory - dark matter - methods: numerical simulations - galaxies: interactions

1 INTRODUCTION

In the standard scenario of structure formation, galaxies are surrounded by extended dark matter haloes, which form by gravitational instability seeded by some initial density fluctuation field $\delta(\vec{x}, z)$. According to the simple spherical collapse model (e.g. Peebles 1980), a halo of mass M collapses at a redshift z when the linear density fluctuation field - smoothed on a scale $R \sim M^{1/3}$ - first exceeds some critical threshold (Press & Schechter 1974; Bond et al. 1991; Lacey & Cole 1993; Sheth & Tormen 2002). Small systems collapse at higher redshifts when the universe was denser, and then merge hierarchically to form larger haloes. Galaxy clusters are at the top of this hierarchy: they represent the most massive virialized structures in the present-day universe, and may host thousands of galaxies. Recent studies,

using high resolution numerical simulations (e.g. Moore et al. 1998; Tormen et al. 1998; Springel et al. 2001), have shown that the cores of subhaloes accreted along the host merging history may survive until the present-time to form the so-called substructure population.

Different studies of galaxy formation and evolution have attempted to correlate such substructures with satellite galaxies, with conflicting results. N -Body simulations of galaxy-size haloes seem to predict more substructures than observed (Moore et al. 1999; Stoehr et al. 2003). A number of different solutions to this ‘substructure problem’ have been suggested, among others early cosmic reionization (Susa & Umemura 2004), mass loss and gas stripping (Kravtsov et al. 2004; Macciò et al. 2009), and a downturn in the power spectrum at small scales (Kamionkowski & Liddle 2000).

From the observational point of view, recent kinematic analyses of Milky-Way satellites (Simon & Geha 2007;

* E-mail: cgiocoli@ita.uni-heidelberg.de

Walker et al. 2009) have shown that, if galaxy formation in low-mass dark matter haloes is strongly suppressed after reionization, the circular velocity function of simulated CDM subhaloes can be brought into approximate agreement with the observed circular velocity function of the Milky Way satellite galaxies (e.g., Koposov et al. 2009). Ishiyama et al. (2008, 2009) claim instead that there is no missing satellites problem if one considers the scatter in the substructure mass function due to the different formation history of the haloes. The idea here is that the Milky-Way and Andromeda haloes reside within an underdense region, so they accreted their substructures at above average redshifts (compared to other objects of the same mass today), and so they are expected to possess fewer satellites (see also van den Bosch et al. 2005).

Knowledge of the substructure population is important, not only for galaxy formation studies, but also for estimating the expected observable γ -ray flux from dark matter particle annihilations within the Milky Way. The expected flux depends strongly on the substructure population, its spatial distribution within the halo, and on the DM particle cross section (Pieri et al. 2008; Diemand et al. 2007; Giocoli et al. 2008b).

The observed thickness of stellar disks in spiral galaxies is another imprint of the substructure population of the host haloes. Semi-analytical models (Benson et al. 2004) and numerical simulations (Kazantzidis et al. 2008, 2009) show that merging events in the central region of the halo are responsible for disk thickening. Hence, the substructure mass function, its redshift evolution and the satellite accretion rate all represent key ingredients for a more complete model of the disk structure of spiral galaxies, not to mention flares, bars, and faint filamentary structures above the disk plane.

Different algorithms have been proposed to identify substructures in simulated dark matter haloes. All these algorithms yield subhalo mass functions that resemble a power-law at the low mass end with a logarithmic slope in the range from -0.8 to -1 (Gill et al. 2004a; Gao et al. 2004; De Lucia et al. 2004; Shaw et al. 2006; Giocoli et al. 2008a; Madau et al. 2008; Wetzel et al. 2009a), both at redshift $z = 0$ and at higher redshifts. In this work we highlight some differences among four such methods and present a new subhalo finder which we believe is useful for studies of galaxy formation and evolution in that it is directly linked to the merger tree of the host halo.

In this paper we focus on the study of the “dark” subhalo population and on its redshift evolution, to help clarify the role of dark matter and its dynamics in the structure formation history. In Section 2 we describe several substructure identification algorithms already in the literature, including the one we will be modifying. Section 3 describes the cosmological N -Body simulation we use, and the required post-processing. Our new algorithm to identify substructures, and an analytic fit to the resulting subhalo mass function is presented in Section 4. Section 5 discusses how the scatter in the substructure mass fraction at fixed mass and at different redshifts correlates with the formation history, and other structural parameters of the halo. A summary and conclusions are given in Section 7. In Appendix A we compare the results of this paper with two previous ones: Giocoli et al. (2008a) and Gao et al. (2004) that studied the substructures population on the same cosmological simulation but

with different algorithms. In Appendix B we propose some fitting functions useful to rescale the virial radius and mass when different definitions of the enclosed virial density are adopted.

2 BACKGROUND

To date, several different algorithms have been proposed to identify substructures within simulated dark matter haloes, and different definitions have been adopted by several authors.

- Ghigna et al. (2000) used an algorithm called SKID. At each simulation snapshot, SKID estimates the density of each particle using a cubic spline kernel; each particle is then moved along the density gradients until it oscillates around a local density maximum. Particles are then linked using a friends-of-friends (FoF) algorithm (Davis et al. 1985), and the groups thus found are pruned iteratively to retain only self-bound particles. However, to obtain the full substructure mass SKID requires a user-defined choice for the linking length to be used by the FoF algorithm. Also Weller et al. (2005) implemented an analogous algorithm to identify substructures by moving particles up density gradients and identifying groups as all particles reaching the same density maximum. In addition, they also implemented a method to identify a hierarchy of subhaloes within subhaloes. Shaw et al. (2007) improved the algorithm of determining the energetically bound components of a subhalo taking into account also all the forces, both internal and external, exerted on the subhalo.

- Springel et al. (2001) developed SUBFIND, which defines ‘subhaloes’ as locally overdense, self-bound particle groups. SUBFIND runs on individual simulation snapshots, but can afterwards reconstruct the full merger tree of each subclump, by using the subhalo information from previous snapshots (Springel et al. 2005; Croton et al. 2006; Harker et al. 2006). The density of each particle (assumed as tracers of the three-dimensional dark matter density field) is estimated using an SPH-fashion scheme: the local smoothing scale is set to the distance of the N_{dens} nearest neighbor, and the density estimated by kernel interpolation over these neighbors. Locally overdense regions are identified by imitating such a lowering of a global density threshold. Any locally overdense region enclosed by an isodensity contour that traverses a saddle point is considered as a substructure candidate. All subhalo candidates are also examined and unbound particles are removed and redistributed. This algorithm has been used and tested by different authors (Gao et al. (2004); De Lucia et al. (2004); Springel et al. (2005)). In particular SUBFIND has been run on the largest existing simulation of the Milky Way (Springel et al. 2008a; Springel et al. 2008b).

- Gill et al. (2004a) and Gill et al. (2004b) used MLAPM (Knebe et al. 2001), an adaptive mesh refinement code for cosmological simulations, to locate substructures in host haloes. To identify haloes and subhaloes at each simulation output, they first build a list of potential centers by storing the centroid of the densest grid point at the end of each grid tree’s “branch”. Assuming that each density peak in the adaptive grid of MLAPM corresponds to the centre of a halo or subhalo, they step outwards in (logarithmically spaced)

radial bins until the mean enclosed overdensity reaches the critical virial value $\Delta_{\text{vir}}(z)$ (Eke et al. 1996; Bryan & Norman 1998), thus defining R_{vir} . However, subhaloes do not extend out to their original virial radius, but rather to some truncation radius R_{trunc} , where an upturn in the radial density profile is detected. This rise is encountered because substructures are embedded in the background of the host halo.

- Tormen et al. (2004) and Giocoli et al. (2008a) developed and optimized the code SURV, which identifies subhaloes within the virial radius of the final host by following their progenitors from the time they were first accreted by the host main progenitor. Hence, SURV differs from the methods discussed above in that it uses prior information based on the merger tree of a host halo at redshift z_0 to identify its subhaloes. For each progenitor halo p that has been accreted onto the main progenitor, SURV identifies a subhalo as the subset of particles that belonged to p at the moment of accretion ($z_{\text{acc}} > z_0$) and are still part of a self-bound entity at z_0 within the corresponding tidal radius. For each subhalo thus identified, SURV stores the accretion time, z_{acc} , the original virial mass (i.e., the mass at z_{acc}), as well as the evolution of its orbital parameters after accretion. In this paper we extend SURV by following all branches of the merger tree (rather than just the main branch), in order to reconstruct the full hierarchy of substructure down to the mass resolution of the simulation (i.e., we aim to identify sub-subhaloes, sub-sub-subhaloes, etc).

3 THE SIMULATION

We used the data from GIF2 (Gao et al. 2004), a cosmological N -Body simulation which is available at <http://www.mpa-garching.mpg.de/Virgo>. The simulation followed the evolution of 400^3 dark matter particles, each of mass $1.73 \times 10^9 h^{-1} M_{\odot}$, in a periodic cube of comoving side $110h^{-1}\text{Mpc}$ within which the background cosmology was ΛCDM with $(\Omega_m, \sigma_8, h, \Omega_b h^2) = (0.3, 0.9, 0.7, 0.0196)$. We made use of 50 snapshots, mostly logarithmically spaced in time between $z = 10$ and $z = 0$. These are sufficiently closely spaced in time that one can reconstruct accurate halo and subhalo merger trees (Tormen et al. 2004; Giocoli et al. 2008a). See Gao et al. (2004) and Giocoli et al. (2008a) for more details about the GIF2 simulation and the post-processing.

3.1 Merger Trees and Substructures

For each simulation snapshot, haloes are identified using a spherical overdensity criterion: first we determine the local dark matter density at the position of each particle, i , by calculating the distance to the tenth closest neighbor, $d_{i,10}$. We assign to each particle a local density $\rho_{i,\text{DM}} \propto d_{i,10}^{-3}$, sort particles in density and take as centre of the first halo the position of the densest particle. We then grow a sphere around this centre, and stop when the mean density within the sphere falls below $\Delta_{\text{vir}}(z)\rho_{\text{crit}}(z)$ as dictated by the spherical collapse model. For a flat universe, this is approximated to better than one percent by

$$\Delta_{\text{vir}}(z) = 9\pi^2 \left(1 + \Omega_m(z)^\beta - \alpha [1 - \Omega_m(z)] \right) \quad (1)$$

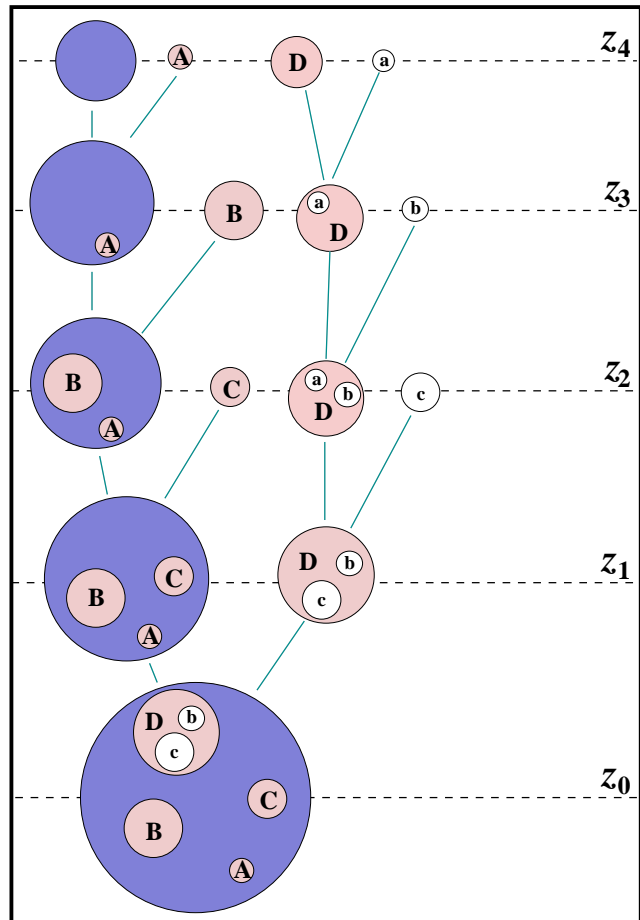


Figure 1. Schematic representation of the merger tree of a dark matter halo along discrete time steps. The dark-grey haloes on the left represents the evolution of the main halo progenitor, which accretes ‘satellite’ haloes A , B , C and D that give rise to a population of subhaloes⁽¹⁾. System D has accreted satellite haloes itself (a , b and c), before it was accreted by the host. Those that survive (b and c) give rise to a population of subhaloes⁽²⁾.

with $\alpha = 0.7076$ and $\beta = 0.4403$ (Stoehr 1999). For the GIF2 cosmology, $\Delta_{\text{vir}} = 97$ times the critical density at $z = 0$, and it increases with redshift, asymptoting to $18\pi^2$ at early times. In Appendix B we present fitting functions that allow halo radius, mass and concentration to be converted to those appropriate for other values of Δ_{vir} .

At this point we assign all particles within the sphere to the newly formed halo, and remove them from the global list. We take the centre of the next halo at the position of the densest particle among the remaining ones, and grow a second sphere. We continue in this manner until all particles are screened. We include in our catalogue only haloes with at least 10 particles within the virial radius; particles not ending up in any halo are considered as ‘field’ or ‘dust’ particles. Hereafter we will refer to the virial mass of a (host) halo thus identified at redshift z as M_z .

To construct merger trees we proceed as follows: for each halo M_{z_i} , identified in the simulation snapshot corresponding to redshift z_i , we define the progenitors at the previous output time (at $z_{i+1} = z_i + \Delta z$) as being all haloes containing at least one particle that at z_i will be in M_{z_i} . The

observation redshift z_0	11.5-12	12-12.5	12.5-13	13-13.5	13.5-14	14-14.5	> 14.5
0	8305 (10230)	3349 (3897)	1186 (1346)	461 (503)	127 (141)	35 (36)	4 (4)
0.5	9347 (11252)	3544 (3940)	1244 (1352)	394 (411)	94 (94)	21 (21)	2 (2)
1	9574 (11115)	3455 (3808)	1095 (1157)	279 (289)	57 (57)	2 (2)	1 (1)
2	8465 (9365)	2461 (2586)	593 (605)	98 (101)	5 (5)	2 (2)	-
4	2847 (2878)	427 (431)	35 (35)	- (1)	-	-	-

Table 1. The number of host haloes in each mass bin and at each ‘observation redshift’ z_0 . Note that we only consider host haloes whose mass never exceeds the mass at $z = z_0$ by more than 10%. The number in parenthesis is the *total* total number of haloes in each mass bin, including those that do not meet this criterion.

progenitor providing the largest mass contribution to the parent halo is termed the *main progenitor*. Starting from a host halo at $z = z_0$, we iterate this procedure back in time, thus obtaining a complete merger tree down to the mass resolution fixed at 10 particles per halo.

Fig. 1 shows a schematic representation of a merger tree to help us define the terminology used throughout the paper. The *main branch* of the merger tree is defined as the branch tracing the main progenitor of the main progenitor of the main progenitor etc... (i.e. the branch connecting the dark grey haloes in Fig. 1). We will use the term *satellites* to refer to all progenitor haloes accreted by the main progenitor, and donating at least 50% of their mass to the host halo at $z = z_0$. In Fig. 1 these are the light grey haloes *A*, *B*, *C* and *D* (as defined before they were accreted onto the main branch). Extending the same definition to each of these satellites haloes, we can go back in time and trace for each satellite its own main branch and satellites. For example, satellite *D* has accreted its own satellites *a*, *b* and *c* at some redshift z_3 , z_2 and z_1 , respectively.

We stress that not all satellites will survive to $z = z_0$: many of them will be destroyed by tidal effects, encounters and other dynamical processes. As an example, satellite *a* in Fig. 1 only survives until $z = z_2$. For this reason, in order to identify substructures at z_0 , at any level of the hierarchy, we need to climb the merger trees of all satellites (at any level of the hierarchy) only up to satellites that will make it to $z = z_0$, but not further. In the example of Fig. 1, we will stop climbing the merger tree of satellite *D* at z_3 , which is the lowest redshift when any possible substructure present inside *D* at $z = z_3$ has no self-bound counterpart at z_0 . We will call *D*(z_3) a *heirless* satellites. In the same spirit, the other heirless satellites in Fig. 1 are *A*(z_4), *B*(z_3), *C*(z_2), *b*(z_3) and *c*(z_2). Their self-bound counterparts at z_0 constitute the substructure population of the host halo, at all levels of the hierarchy. In what follows we use subhaloes^(*i*) to refer to the *i*th level of this substructure hierarchy, with $i = 1$ corresponding to the first order of subhaloes, i.e. the ones accreted directly by the main progenitor. Hence, in Fig. 1 haloes *A*, *B* and *C* are subhaloes⁽¹⁾, while *b* and *c* make up the population of subhaloes⁽²⁾ of the host halo at $z = z_0$. We will use the term ‘substructures’ to refer to subhaloes of the entire hierarchy ($i = 1, 2, 3, \dots$). The mass of a substructure at z_0 is defined by the clump of particles, originally belonging to a heirless satellite, that at $z = z_0$ are still self-bound within the tidal radius of that clump.

This procedure is iterative, because the tidal radius itself is defined using the self-bound mass of the clump.

To implement this algorithm in our code, assume that we have a simulation with N snapshots, and let z_i be the redshift of snapshot i . Let z_N and z_0 be the redshifts of the earliest and final snapshot, respectively. Starting from the population of subhaloes identified by SURV at z_0 , we proceed along the following steps:

- given a subhalo $s(z_0)$, accreted as satellite at $z_i > z_0$, we climb one step along its own merging history tree and read the information about its progenitors at z_{i+1} ;
- for each of these progenitors, we trace the position of its particles to z_0 , and see if there is a self-bound clump within its own tidal radius (as defined in Tormen et al. 1998);
- if at least two progenitors identified at z_{i+1} (the main progenitor and another satellite) have a counterpart clump $s'(z_0)$ made of at least 10 self-bound particles, this means that $s(z_0)$ has substructures inside itself. We therefore update the previous subhalo catalogue by replacing $s(z_0)$ with the counterparts $s'_1(z_0)$, $s'_2(z_0)$, ..., of the survived progenitors. Notice that one of these progenitors will always be the main progenitor of $s(z_0)$, so this procedure will certainly re-identify the core of $s(z_0)$. Any other counterpart $s'_i(z_0)$ will identify a new subhalo at a further level of the substructure hierarchy.
- if, of all progenitors identified at z_{i+1} , only the main progenitor has a self-bound counterpart at z_0 , this means that $s(z_0)$ has no further levels of substructure, and the (satellite) main progenitor of $s(z_0)$ at z_i is a heirless satellite. In this case we leave the subhalo $s(z_0)$ as is, and proceed to the next one in the catalogue.

After we have scrutinized all subhaloes once, we start again and consider the updated subhalo catalogue (which now contains new subhaloes at one further level of hierarchy). We repeat the steps described above, skipping however the subhaloes coming from heirless satellites, and split any new subhalo as described. We iterate the whole procedure: each time we replace the subhaloes - which at z_0 may be split in two or more self-bound sub-units - with the sub-units themselves. At some point, all subhaloes at z_0 will be the counterpart of some heirless satellite. We call the resulting population a catalogue of *substructures*. This catalogue is the one we use for our investigation.

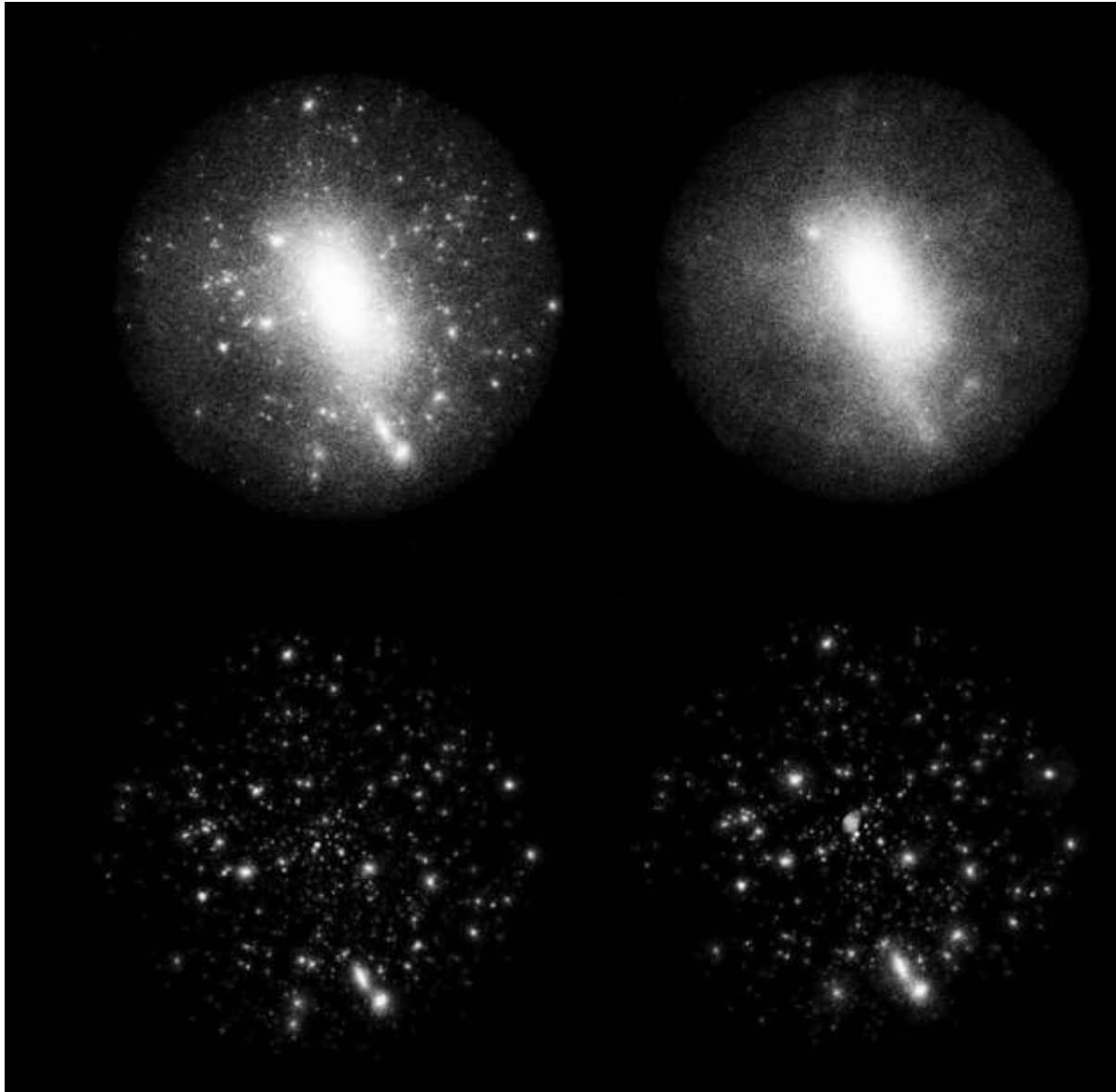


Figure 2. Dark matter particle distributions for the most massive halo ($M = 1.85 \times 10^{15} h^{-1} M_{\odot}$) in the GIF2 run at $z = 0$, the radius of the sphere is $2.54 h^{-1} \text{Mpc}$. Top left: all dark matter particles within the virial radius. Top right: diffuse dark matter not associated with any substructure. Bottom left: substructures, i.e. self-bound particles belonging to heirless satellites haloes (see the main text for more details). The particle distribution in the top right and bottom left sum to give that in the top left. Bottom right: subhaloes⁽¹⁾, i.e. self-bound particles from satellite haloes accreted directly by the main progenitor (Giocoli et al. 2008a). The two bottom panels only show substructures and subhaloes⁽¹⁾ with at least 10 particles. Clumps at radii $r < 0.05 R_{\text{vir}}$ are not well defined, and were excluded from the study by Giocoli et al. (2008a) and hereafter.

4 RESULTS

Figure 2 shows the dark matter distribution for the most massive halo found in the GIF2 run at $z = 0$. The top left panel shows all particles inside the virial radius. The top right panel shows halo particles not bound to substructures (dust particles). The bottom left panel shows particles bound to substructures (i.e. the final result of our procedure). The particle distribution shown in the top left panel is the sum of that in this panel and that shown in the top right. The bottom right panel shows the particles bound to subhaloes⁽¹⁾ (i.e. the starting point of our procedure); these

are the objects identified by Giocoli et al. (2008a). A comparison between the two lower panels shows that the largest subhaloes⁽¹⁾ are split into smaller and smaller substructures as we proceed further along the merger tree, until we reach the heirless satellites. Note that the total mass in the two bottom panels is different for two reasons. First, some of the particles in the Giocoli et al. (2008a) subhaloes are no longer bound to any of the substructures. Second, some substructures found by our new algorithm (bottom left) were not identified as subhaloes⁽¹⁾ (bottom right). While the old algorithm SURV only follows the most massive piece, our

new algorithm identifies all these pieces as satellites of the original system. Figure A1 shows the net change in the mass fraction associated with substructures.

In what follows we discuss the substructure of the host haloes as function of mass and redshift. We consider five values of z_0 : 0, 0.5, 1, 2 and 4, and for each, we consider seven mass bins. Throughout we only use host haloes whose main progenitor never exceeds the final mass M_{z_0} by more than 10%. Table 1 lists the number of haloes in each of these bins. Note that substructures in the innermost region (within 5% of the virial radius) are excluded from further study, as their identification is uncertain due to the extreme density of the host.

The resulting substructure mass functions are shown in Figure 3; masses are in units of the virial mass of the host halo. The various symbols and line types in each panel show results for different host masses. The solid curve (same in each panel) shows the *unevolved* subhalo mass function (equation 2 of Giocoli et al. 2008a), i.e., the mass function of progenitor haloes accreted onto the main branch of the merger tree:

$$\frac{dN(m_{\text{sb}}|M)}{d \ln m_{\text{sb}}} = N_0(M_{z_0}) \xi^\alpha \exp(-\beta \xi^3) \equiv \xi f(\xi), \quad (2)$$

with $\xi = m_{\text{sb}}/M_{z_0}$, $\alpha = -0.8$, $\beta = 12.2715 \approx 0.43^{-3}$ and normalization $N_0(M_{z_0}) = 0.18$. Note that the normalization is independent of both the mass of the host halo and the redshift at which it was identified even though our notation suggests otherwise. The reason for our notation will become clear shortly. For comparison, the dashed line shows a power law with slope $\alpha = -0.9$ and normalization $N_0 = 0.03$: it is steeper than the solid line. Performing least squares interpolation on the linear trend of the substructure mass functions we notice that this value of the slope is in agreement with the value estimated in the more massive bins, while it tends to overestimate a little the slope in the smaller ones. This because subhaloes in the latter are mainly preserved and not split in sub-subhaloes.

Giocoli et al. (2008a) have shown that, even after tidal stripping, the evolved mass function of subhaloes⁽¹⁾ (i.e. for the objects in the bottom right panel of Figure 2) has the same shape as the unevolved one (e.g., power law slope $\alpha = -0.8$ at small m_{sb}/M_{z_0}). I.e., the mass function for objects like those in the bottom right panel of Figure 2 is given by sliding the solid curve downwards by an amount that depends on M_{z_0} (and z_0). The reason for this is not completely straightforward, since mass-loss alone would be associated with sliding to the left, not down. As discussed in van den Bosch et al. (2005), this happens because the mass loss depends on the time spent by a satellite within the potential well of its host, and Giocoli et al. (2008a) showed that the mass function of objects which accreted before and after the main progenitor had acquired half the final mass of the halo are *both* described by equation (2), but with different normalization factors (lower by factors of 0.57 and 0.43 respectively). Crudely speaking, all the subclumps accreted prior to the half-mass time have been erased completely, and all those accreted later are still present, but they have been stripped. So, crudely speaking the evolved mass function should be given by taking equation (2), but with normalization lower by a factor of 0.43, and then shifting it to the left. To match amplitudes, the typical shift is about a factor

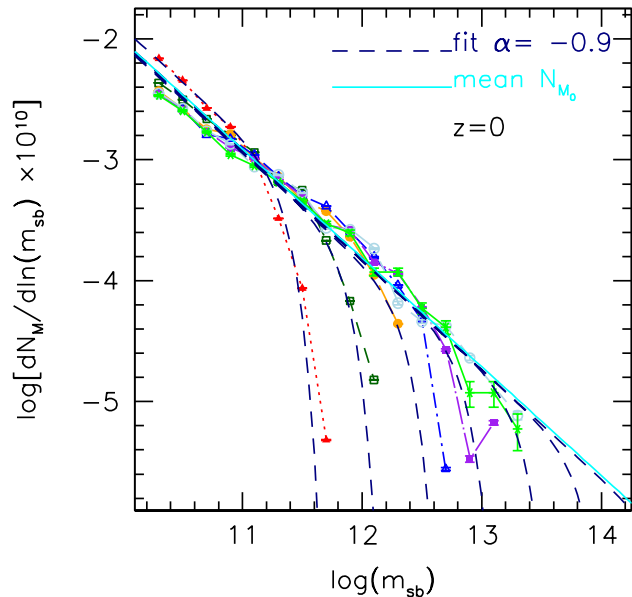


Figure 4. Substructure mass function per unit host halo mass (in units of $10^{10} h^{-1} M_\odot$). Different data points refer to the same mass bins as in Figure 3. The solid line shows a power law distribution with slope $\alpha = -0.9$ and a mean normalization computed over the different mass bins (see the text for more details). The dashed lines show the fit to the data for each mass bin plus the high mass exponential cut-off.

of 3. However, because low mass objects typically formed at higher redshifts, their subhaloes have suffered more mass loss, so the shift is larger for smaller M_{z_0} . Over the mass range where the mass function resembles a power law, the leftwards shift resembles a downwards shift in the normalization of equation (2), so the number of subhaloes of a given m_{sb}/M_{z_0} is larger for larger M_{z_0} . In the next section, we show that the scatter around this relation is also directly related to the halo assembly process.

The symbols in Figure 3 do not show this evolved subhalo mass function. Rather, they show the substructure mass function associated with our new algorithm (i.e., for the objects shown in the bottom left panel of Figure 2). Notice that this function has a steeper slope ($\alpha = -0.9$) than that for the subhaloes⁽¹⁾ (at least in the most massive host haloes). However, equation (2) still provides a good description of the full shape, if we simply set $\alpha = -0.9$, keep $\beta = 12.2715$, but now allow the normalization $N_0(M_{z_0})$ to depend on the mass (and, we show later, on z_0) of the host halo.

Figure 4 shows the substructure mass function if one does not normalize all m_{sb} by M_{z_0} . Namely, it shows

$$\frac{dN_M}{d \ln m_{\text{sb}}} \equiv \frac{m_{\text{sb}}}{M_0} \frac{dN}{dm_{\text{sb}}} = N_{M_0} m_{\text{sb}}^\alpha \exp(-\beta \xi^3), \quad (3)$$

where the normalization factor is

$$N_{M_0} = \frac{N_0(M_{z_0})}{M_0^{1+\alpha}}. \quad (4)$$

The dashed curves show this expression with $\alpha = -0.9$ and normalization determined by chi-square minimization to the data for each bin in M_0 . Figure 5 shows that, with the exception of the lowest mass bin, $\log N_{M_0} = -3.03$ almost independent of mass. We believe the lowest mass bin, for

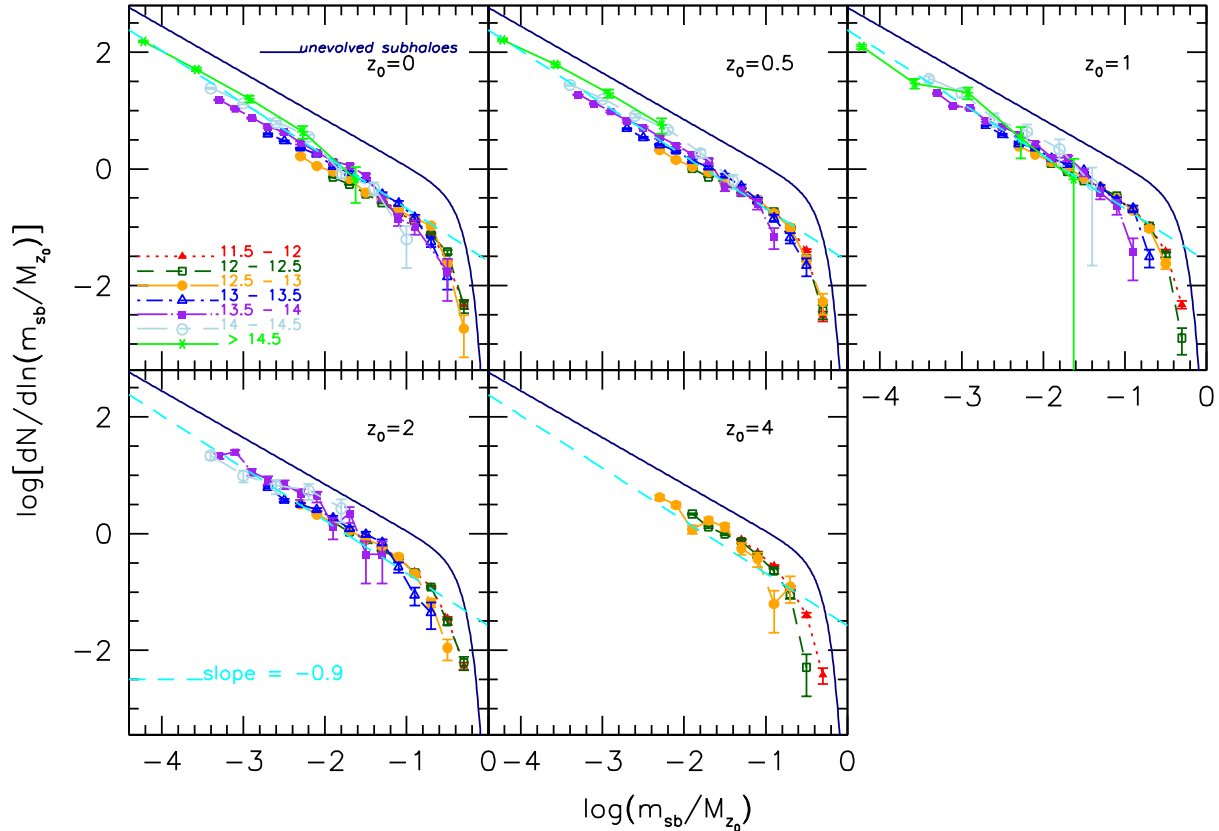


Figure 3. Substructure mass functions at five different redshifts z_0 as indicated. We divide the host haloes in seven different mass bins and plot the mass function (in units of the host halo mass M_{z_0}) at that redshift. In each panel the dashed line shows a power law with slope $\alpha = -0.9$ and normalization $N_0 = 0.03$ that fits well the data points at $z_0 = 0$. For comparison, the solid curve represents the *unevolved* subhalo mass function (equation 2).

which the haloes have the fewest particles, is compromised by discreteness effects: the substructure mass loss rates of the objects in this bin are rather discontinuous.

The substructure population in this GIF2 simulation has also been studied by Gao et al. (2004). They used a different post-processing pipeline and their algorithm to identify substructures, SUBFIND, is different from ours. So it is remarkable that our mass functions agree rather well: we both find $\alpha = -0.9$. However, our normalizations are different: they find -3.2 whereas we find -3.03 . This can be traced to the fact that we define haloes as being $\Delta_{\text{vir}}(z)\rho_{\text{crit}}(z)$, whereas they fix $\Delta_{\text{vir}} = 200$. In effect, their haloes are smaller and less massive than ours (Appendix B shows that the volume $V_{200} \approx 0.4 V_{\text{vir}}$ at $z = 0$). Hence, at the same numerical value for the halo mass, our haloes are ‘effectively’ more massive than theirs, which means smaller formation redshifts, and hence higher mass fractions of surviving substructure. We believe this to be responsible for the difference in normalization. Appendix A gives a more detailed discussion of the differences between our new algorithm, that of Gao et al. (2004), and that of Giocoli et al. (2008a).

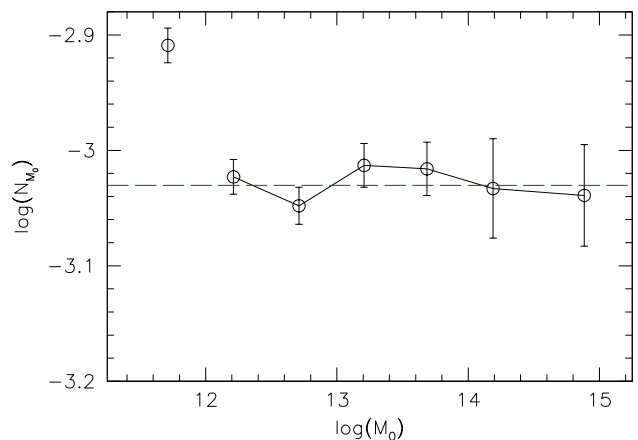


Figure 5. Host halo mass dependence of the normalization factor N_{M_0} in eq. (3) at $z_0 = 0$. The error bars were obtained by bootstrapping the host halo sample in each mass bin and computing the rms of the normalization factors obtained for the bootstraps. The dashed line in the top panel shows the mean weighted by the errors of the data points excluding the smallest mass bin (see the main text for more details).

5 MASS FRACTION AND SUBSTRUCTURES

In this section, we show how the substructure mass fraction correlates with other properties of the halo (mass, concentration, formation time). Most of these are expected – our results quantify the trends. We then study how the number of substructures depends on the redshift at which the host halo is identified.

5.1 Correlations with mass, formation time, and concentration

The structure of a dark matter halo is related to its accretion history (Zhao et al. 2009, and references therein). To quantify the different halo assembly histories we will use the formation time, defined as the earliest time when the main progenitor reaches a mass that is half of the final mass of the halo (e.g., Lacey & Cole 1993). Previous work has shown that massive objects formed more recently (e.g., Lacey & Cole 1993; van den Bosch 2002; Sheth & Tormen 2004; Giocoli et al. 2007). Systems that form at high redshift, when the universe was denser, are denser. This, with the fact that massive objects formed more recently gives rise to the mass concentration relation (Navarro et al. 1996; Bullock et al. 2001; Macciò et al. 2007; Neto et al. 2007; Zhao et al. 2009) and its scatter. In addition, using extended Press-Schechter theory, van den Bosch et al. (2005) showed that the unevolved subhalo mass function is universal, which was confirmed with numerical simulations by Giocoli et al. (2008a). Hence, they predicted that less massive haloes, which on average form earlier (i.e., accrete their subhaloes earlier), would have less surviving substructure at the present, simply because their substructure would have been exposed to tidal stripping for a longer duration. van den Bosch et al. (2005) thus predicted a correlation between f_s and mass, but also that the scatter in f_s at fixed mass be correlated with the formation time of the halo.

To check this, for each halo we computed

$$f_s = \frac{\sum_i m_{sb,i}}{M_0},$$

and, for each mass bin,

$$\langle f_s \rangle = \frac{\sum_{j=1}^{N_{haloes}} f_{s,j}}{N_{haloes}}.$$

When computing these sums, we considered all substructures with at least 10 self-bound dark matter particles that were more than $0.05R_{vir}$ from the center of the host halo.

Figure 6 shows this mean substructure mass fraction at $z = 0$ for a range of host halo masses. The open circles show results for the full set of haloes in each mass bin, whereas triangles and diamonds show the subset which formed below and above the mean formation redshift (for that mass). At $z = 0$, we have 13467 (7158), 4407 (3898), 1834 (1515), 610 (576), 215 (246), 72 (55), 18 (17) and 2 (2) haloes with a formation redshift higher (lower) than the mean, for our seven mass bins. This shows that the normalization factor N_0 of the substructure mass function depends on M_0 and on the formation redshift z_f . For a given mass, lower formation redshift translates into a higher substructure mass fraction and smaller smooth dark matter component $M_0(1 - f_s)$. The three dashed lines show least squares fits to the three sets

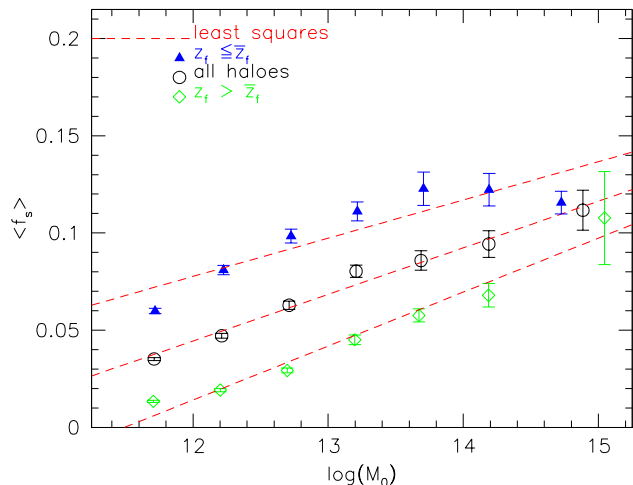


Figure 6. Fraction of present-day host halo mass in substructures. Open circles show the substructure mass fraction considering all haloes in each of the seven mass bins. Filled triangles and open diamonds represent the mean substructure mass fraction considering only haloes with a formation redshift lower and higher than the mean in the corresponding mass bin, respectively. The error bar shows the rms. The dashed lines show least squares fits to the three sets of data points.

of data points:

$$\langle f_s \rangle = a \log(M_0) + b, \quad (5)$$

where a and b for the lines going from the top to bottom in Figure 6 we have:

$$(a, b) = \begin{cases} (0.020 \pm 0.004, -0.16 \pm 0.06) & \text{if } z_f \leq \bar{z}_f, \\ (0.024 \pm 0.001, -0.24 \pm 0.02) & \text{for all haloes,} \\ (0.027 \pm 0.002, -0.32 \pm 0.03) & \text{if } z_f > \bar{z}_f. \end{cases}$$

Figure 7 shows another way of presenting the joint distribution of halo mass, formation time and f_s . In this case, we study the correlation between f_s and z_f for different masses. The black diamonds show this correlation for all haloes more massive than $10^{11.5} M_\odot/h$, the dashed line shows a least squares fit:

$$\log \langle f_s \rangle = (-3.133 \pm 0.13) \log(1 + z_f) - (0.48 \pm 0.05), \quad (6)$$

and the other symbols show the correlation for narrow mass bins. Notice that the substructure mass fraction is tightly correlated with the halo assembly redshift for haloes of all masses, indicating that, to good approximation, we can write that $f_s = f_s(z_f)$. The fact that this $f_s - z_f$ correlation depends little on mass M_0 , whereas the $f_s - M_0$ correlation depends strongly on z_f indicates that the $f_s - M_0$ correlation is almost entirely determined by the $f_s - z_f$ and $z_f - M_0$ correlations. From the figure we notice also that for haloes formed quite recently, a high value of the substructure mass fraction indicate that they have undergone a recent almost 1:1 major merging event. This can also be understood if we consider the conditional distribution of masses at formation studied by Sheth & Tormen (2004). In this work they show that the distribution is tightly peaked around 1/2 for large formation redshift (since there were few progenitors of large mass at high- z), whereas it is much broader for lower z_f : so low z_f means more recent 1:1 mergers.

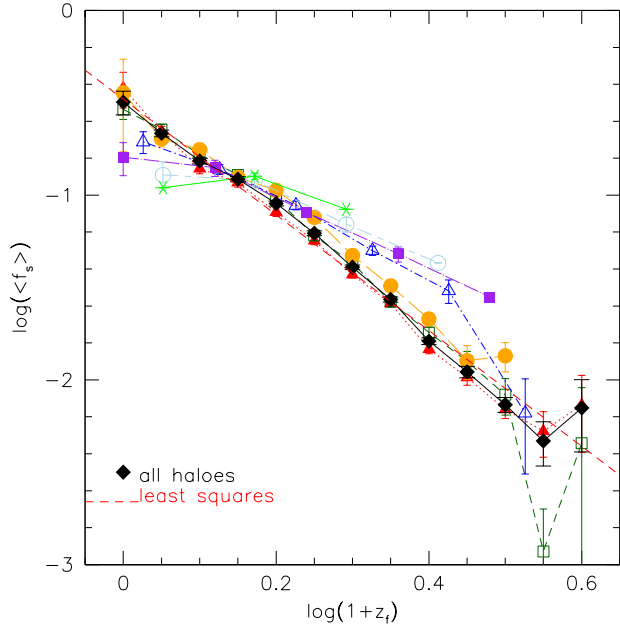


Figure 7. Correlation between the substructure mass fraction and host halo formation redshift. Different symbols show results for the mass bins as in Figure 3. Filled diamonds show the relation averaged over all haloes more massive than $10^{11.5} M_{\odot}/h$ at $z = 0$; dashed line shows a least squares fit.

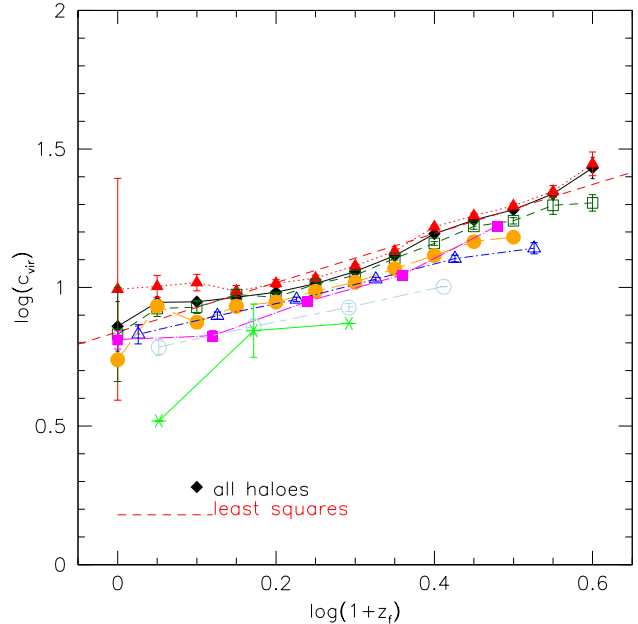


Figure 9. Concentration-formation redshift correlation. Different symbols and line styles show results for different mass bins (as in Figure 7). Dashed line shows a least squares fit to the relation traced by the filled diamonds, which show the average over all haloes at $z = 0$.

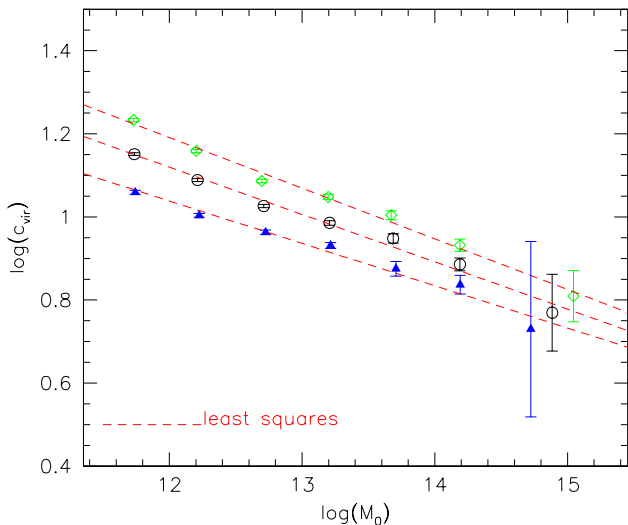


Figure 8. Mass-concentration relation at $z = 0$. Open circles show the mean for the full sample at each mass; filled triangles and open diamonds show this relation for haloes with formation redshifts that are lower and higher than the mean (similar to Figure 6). Dashed lines show least squares fit to these relations.

Halo formation times are not observable, so it is interesting to see if halo substructure correlates with other structural properties. Halo concentrations are potentially observable, and are known to correlate with mass and formation time (e.g. Navarro et al. 1997; Wechsler et al. 2002; Zhao et al. 2009). Figures 8 and 9 show these relations in our simulation. More massive haloes are less concentrated; at fixed mass, the objects which formed at higher redshift

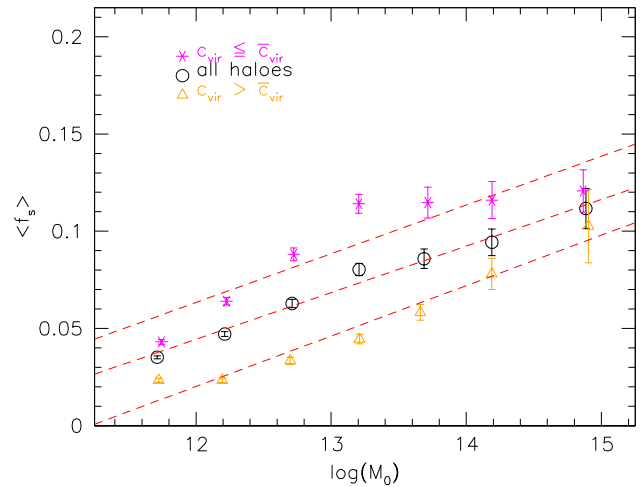


Figure 10. Dependence of mass fraction in substructure on host halo mass and concentration. Open circles show the full sample, triangles and stars show the average over systems with above and below average concentrations for the mass bin. Dashed lines show least squares fits to these trends.

are more concentrated. Different data points refer to various mass bins, as in previous figures, and error bars represent the rms around the mean value. We estimate the halo concentration $c_{\text{vir}} = R_{\text{vir}}/r_s$ fitting the spherical density distribution with an NFW profile. In Figure 8 the three lines show

$$\log(c_{\text{vir}}) = a \log(M_0) + b \quad (7)$$

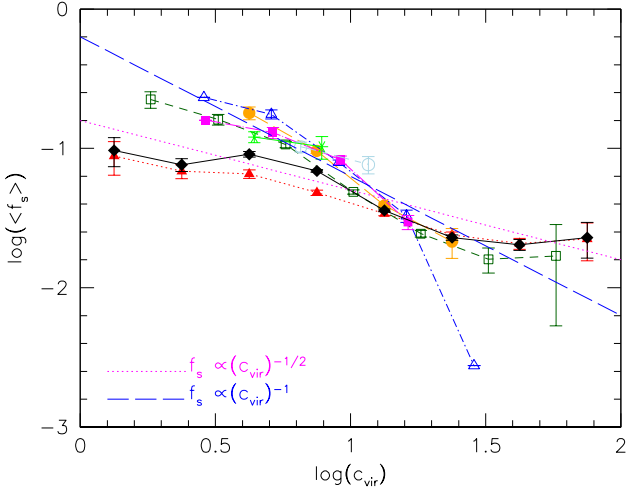


Figure 11. Dependence of mass fraction in substructure on host halo concentration and mass. Symbols and line styles are for different host halo masses (same as Figure 7).

with

$$(a, b) = \begin{cases} (-0.102 \pm 0.008, 2.26 \pm 0.10) & \text{if } z_f \leq \bar{z}_f, \\ (-0.114 \pm 0.006, 2.49 \pm 0.08) & \text{for all haloes,} \\ (-0.122 \pm 0.005, 2.65 \pm 0.07) & \text{if } z_f > \bar{z}_f. \end{cases}$$

In Figure 9 the dashed line shows the least squares fit to all masses. However because the normalization of this correlation depends only weakly on host halo mass, it fits the smallest mass bin, which dominates the numbers.

Figure 10 shows the result of remaking Figure 6, but now replacing host halo formation time with concentration. This shows that, at fixed halo mass, more concentrated haloes have smaller substructure mass fractions. The three dashed lines show the least squares fits to the data points where

$$(a, b) = \begin{cases} (0.251 \pm 0.005, -0.24 \pm 0.07) & \text{if } c_{vir} \leq \bar{c}_{vir}, \\ (0.024 \pm 0.001, -0.24 \pm 0.02) & \text{for all haloes,} \\ (0.026 \pm 0.003, -0.29 \pm 0.03) & \text{if } c_{vir} > \bar{c}_{vir}. \end{cases}$$

Figure 11 shows a similar remake of Figure 7; f_s decreases as concentration increases, approximately independent of halo mass. If we ignore the smallest mass bin, which is most affected by the mass resolution of the simulation, then data points are well-fitted by an inverse correlation between the mass fraction and the concentration of the host halo.

5.2 Redshift dependence

At fixed host halo mass the number of substructures depends on the redshift at which the halo was identified: it is larger at higher redshift. Although they did not emphasize this aspect, Angulo et al. (2008) showed that the subhaloes of hosts identified as being 200 times the critical density in the Millennium simulation using SUBFIND show a similar trend.

Substructure abundance depends on how much stripping has occurred, since this is what changes the universality of the unevolved subhalo population. This stripping

depends on how long a satellite has spent inside its host, and on the dynamical timescale within the host (van den Bosch et al. 2005; Giocoli et al. 2008a). These timescales, that represent the time over which changes in one part of a body can be communicated to the rest of that body, depend on when the host halo is identified ($\tau_{\text{dyn}} \propto \rho_{\text{vir}}^{-1/2}$), so this may be why the higher redshift hosts have more substructures. If we use T to denote the ratio of these two timescales ($T \equiv (t(z) - t_{\text{acc}})/t_{\text{dyn}}(z)$), then large values of T should be associated with more stripping. The top panels of Figure 12 show the distribution of T for substructures in different host halo masses (right to left) identified at two redshifts, $z_0 = 0$ and 2 (solid and dashed histograms). This shows that, for host haloes observed at higher redshift the distribution of T peaks at lower values. Substructures in these systems that have spent less time in the potential well of their host suffer less tidal stripping than those in present-day hosts (of the same mass). The bottom panels show the correlation between the survived mass fraction $m_{\text{sb}}(z_0)/m_{\text{vir}}(z_{\text{acc}})$ and T . As discussed in van den Bosch et al. (2005) and Giocoli et al. (2008a), when the instantaneous mass loss rate does not depend on the host halo mass, then the retained mass fraction decreases as $\exp(-T)$.

5.3 Poisson model for substructure abundance

Figure 13 shows how the mean number of substructures scales with host halo mass, again only counting substructure with ten particles or more (i.e., $m_{\text{sb}, \text{min}} = 1.73 \times 10^{10} h^{-1} M_{\odot}$). The dashed line shows the result of fitting

$$\langle N_s \rangle = A_0 (m_{\text{sb}, \text{min}}) M_0^{\beta}, \quad (8)$$

to the measurements. A least squares fit returns $\beta = 0.97 \pm 0.03$ and $\log(A_0) = -11.79 \pm 0.34$. Of course, this normalization factor A_0 depends on the smallest substructure mass considered, but $\beta \approx 1$ is consistent with the fact that the normalization constant N_{M_0} in equation (3) is independent of M_0 . The other panels of Figure 13 show the second and third factorial moments of this distribution: $\langle N_s(N_s - 1) \rangle$ and $\langle N_s(N_s - 1)(N_s - 2) \rangle$. If the scatter around the mean were Poisson, these would equal $\langle N_s \rangle^2$ and $\langle N_s \rangle^3$ respectively. Evidently, our substructure counts deviate from the Poisson model only slightly (by a factor of $\sim 5\%$ at large masses, and slightly increasing toward small ones). Interestingly, a similar trend was found by van den Bosch et al. (2005) using merger trees constructed using extended Press-Schechter theory.

Figure 14 shows how the mean number of satellites (more massive than $1.73 \times 10^{10} h^{-1} M_{\odot}$) depends on the redshift at which the host halo was identified. Different symbols show counts in haloes at $z_0 = 0, 0.5, 1, 2, 4$. Notice that, for the reasons discussed earlier, at a given host mass, the mean counts are higher for the hosts identified at higher redshift, but that the curves are parallel to one another. The higher number of substructures at high redshift can also be related to an increase in the galaxy merger probability (Wetzel et al. 2009b; Hester & Tasitsiomi 2009) and have implications for galaxy formations and mergers. We showed previously that the substructure mass fraction f_s is anti-correlated with halo concentration c , approximately independent of halo mass. For a given host halo mass, c is smaller at high redshift (e.g. Zhao et al. 2009). Hence, if the $f_s - c$ anti-correlation is the

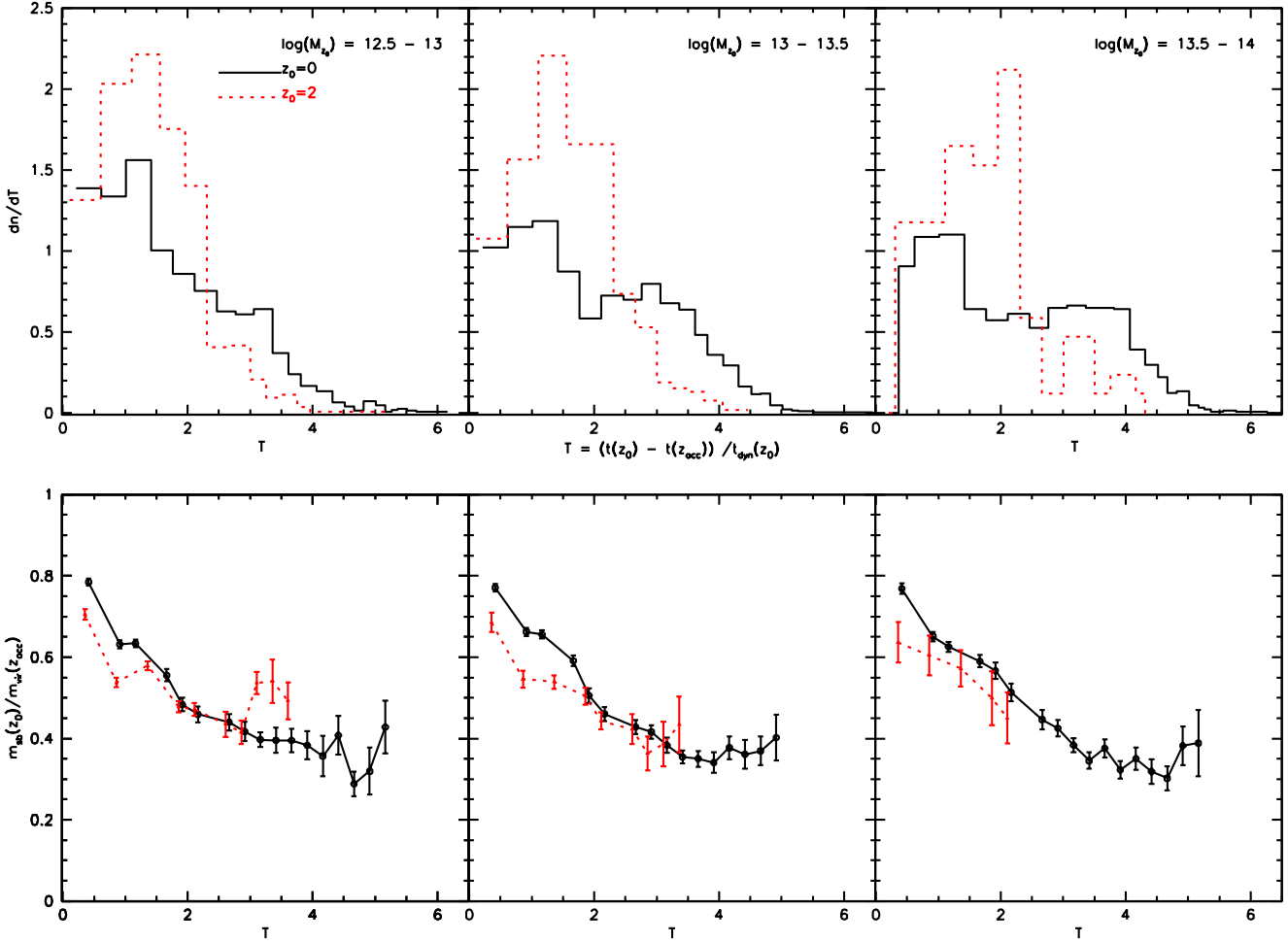


Figure 12. Top panels: Distribution of the time spent by substructures in their host haloes (i.e. since they were accreted), in units of the dynamical time scale at $z_0 = 0$ (solid) and $z_0 = 2$ (dashed). The three panels show results for three bins in host halo mass. Bottom panels: Retained mass fraction for substructures which have survived within their host haloes as a function of (scaled) time, for the same two choices of z_0 and for the same three bins in host mass.

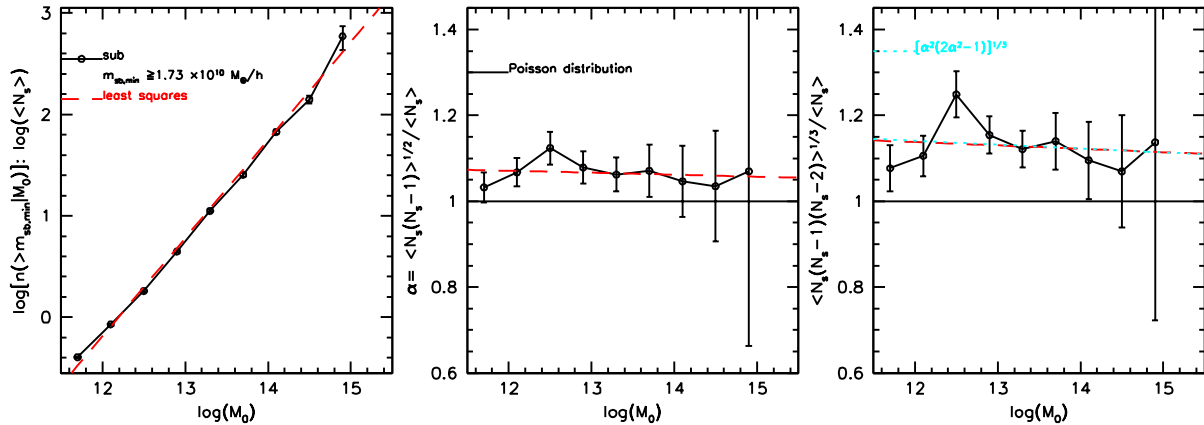


Figure 13. First three factorial moments of the substructure counts as a function of host halo mass. Only substructures with more than 10 self-bound particles, and further than $0.05R_{vir}$ of the host halo center were counted. A Poisson distribution would have value unity in the middle and right-most panels.

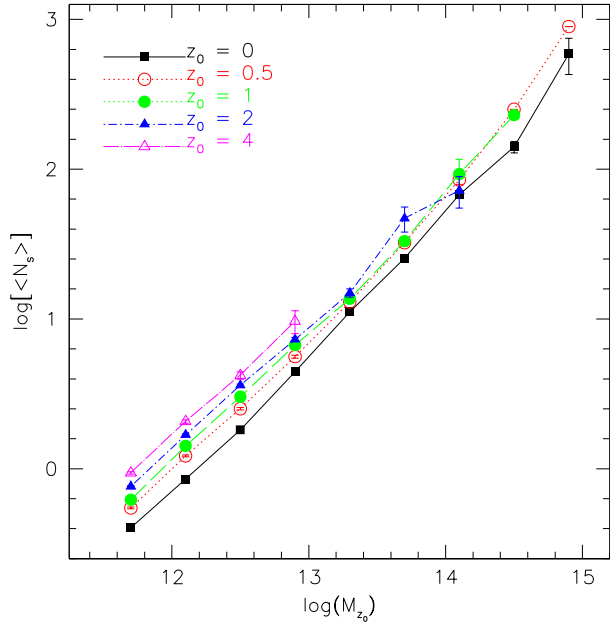


Figure 14. Dependence of the mean number of satellites more massive than $1.73 \times 10^{10} h^{-1} M_{\odot}$ on halo mass, and on the redshift at which the halo was identified. At fixed mass, host haloes identified at higher redshift have more substructures.

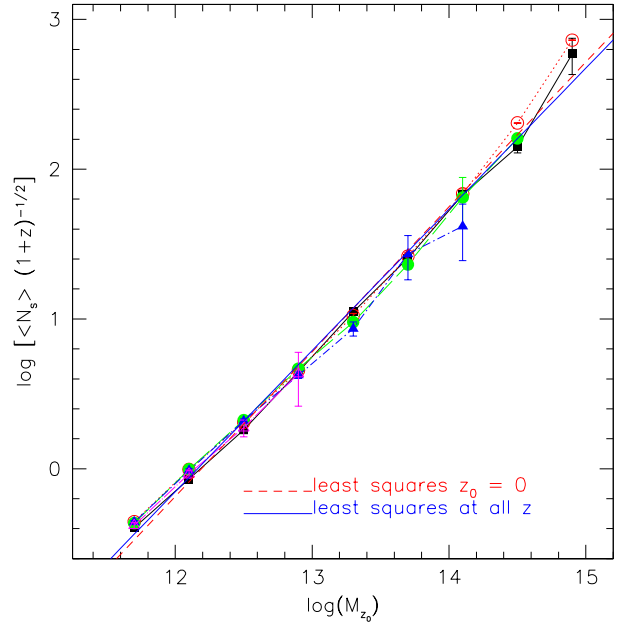


Figure 16. Same as previous figure, but now rescaled by a factor which reflects the anti-correlation between substructure fraction and halo concentration, and the redshift dependence of the halo concentration.

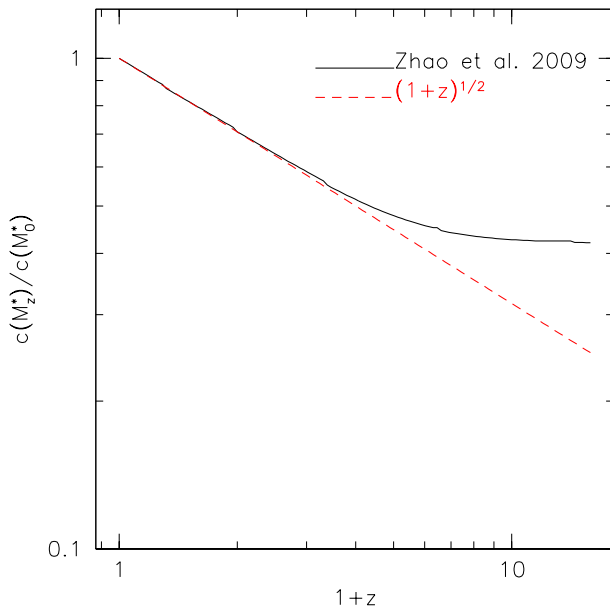


Figure 15. Redshift evolution of the concentration of an M_* -halo (here shown in units of the concentration of M_* haloes at $z = 0$) as predicted by the model by [Zhao et al. \(2009\)](#).

same whatever the redshift at which the host halo is identified, then one expects f_s to be larger at high redshifts, in qualitative agreement with the trend shown in Figure 14.

The hypothesis that the $f_s - c$ anti-correlation does not evolve allows us to be more quantitative, provided that we have a model for how halo concentrations depend on the redshift at which they were identified. [Zhao et al. \(2009\)](#)

describe an accurate model for this, in which a halo's concentration is related to the time at which its main progenitor first assembled 4% of its final mass. We used their model to make Figure 15, which shows the concentration of an M_* halo as a function of redshift z . (I.e., M_* represents the typical halo mass at redshift z , defined by $S(M_z^*) = \delta_c(z)^2$, where $\delta_c(z)$ is the critical overdensity required for spherical collapse at z and $S(M)$ is the variance in the linear fluctuation field when smoothed with a top-hat filter which contains mass M . Thus, M_* is smaller at higher redshift.) This shows that, between $z = 0$ and 4, $c(M_*(z))/c(M_*(0)) \propto (1+z)^{-1/2}$: although $M_*(z)$ is smaller at high redshift, so too is its concentration.

Since $f_s \propto c^{-1}$ at $z = 0$ (Figure 11), the hypothesis that the $f_s - c$ anti-correlation does not evolve suggests that the typical value of f_s at some z_0 will be proportional to $c(M_*(z_0))^{-1}$. Therefore, subhalo counts at z_0 should lie above those at $z = 0$ by a factor of $[c(M_0^*)/c(M_{z_0}^*)] \approx (1+z_0)^{1/2}$. Figure 16 shows the result of dividing the z_0 counts shown in Figure 14 by $(1+z_0)^{1/2}$: this does indeed bring the counts at different z_0 into good agreement with one another. To highlight how well this works, Figure 17 shows the analogue of Figure 5 but for these rescaled counts (symbols and line types as in Figure 14): the rescaled counts are much less redshift-dependent, suggesting that our crude accounting for the effects of the $f_s - c$ correlation on subhalo abundances is reasonably accurate.

6 GLOBAL MASS FUNCTION OF SUBSTRUCTURES

The mass function of substructures, integrated over all host haloes, plays an important role in models which relate sub-

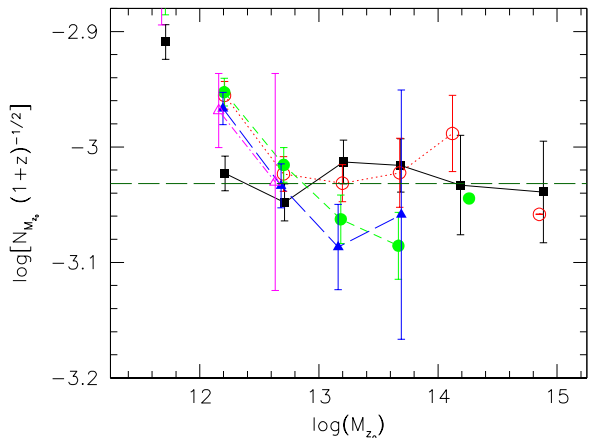


Figure 17. Rescaled normalization factor for the number of substructures per host halo mass, shown in the same format as Figure 5. Different symbols are for host haloes identified at different redshifts z_0 (as in Figure 14).

structures to galaxies (Cooray & Sheth 2002) and to the expected gravitational lensing signal on small scales (Sheth & Jain 2003; Macciò & Miranda 2006; Natarajan et al. 2007; Meneghetti et al. 2007). The global substructure mass function can also be useful for modeling the γ -ray background due to dark matter particles annihilation (Fornengo et al. 2004; Giocoli et al. 2008b, 2009). We now have the necessary ingredients to estimate this quantity:

$$\begin{aligned} \frac{dn(m_{\text{sb}})}{d \ln m_{\text{sb}}} &= \int_{m_{\text{sb}}}^{\infty} \frac{dN(m_{\text{sb}}|M)}{d \ln m_{\text{sb}}} \frac{dn(M)}{dM} dM \\ &= N_{M_0} (1+z)^{1/2} (m_{\text{sb}})^{\alpha} \\ &\quad \times \int_{m_{\text{sb}}}^{\infty} dM \frac{dn(M)}{d \ln M} \exp(-\beta \xi^3) \end{aligned} \quad (9)$$

where dn/dM denotes the comoving number density of dark matter haloes. The histograms in Figure 18 show the result of performing this integral by using equation (2) with $\alpha = -0.9$, $\beta = 12.2715$, the rescaled normalization from Figure 17 for $dN(m|M)/dm$, and the Sheth & Tormen (1999) expression for the mass function of the hosts, dn/dM , at $z = 0, 0.5, 1, 2, 4$ (top to bottom). The short-dashed curves show dn/dM at these same redshifts.

Because of the exponential cutoff in the subhalo mass function, equation (9) cannot be integrated analytically. However, we have found that $y(m_{\text{sb}}) \equiv m_{\text{sb}} dn(m_{\text{sb}})/d \ln m_{\text{sb}}$ is well fit by

$$y(m_{\text{sb}}) = A_0 m_{\text{sb}}^{\eta} \exp \left[- \left(\frac{m_{\text{sb}}}{\bar{m}_0} \right)^{\gamma} \right]. \quad (10)$$

A similar functional form has been used to fit galaxy velocity dispersions (Sheth et al. 2003), so our parametrization is intended to help clarify the connection between galaxies and halo substructure. To determine the parameters A_0 , η , γ and \bar{m}_0 , we perform a least-squares fit to the log of the counts at the small mass end: this determines the slope η and zero-point a_0 of the power law at small masses. We set $A_0 = 10^{a_0}$, and we estimate the other two parameters, γ and \bar{m}_0 , by

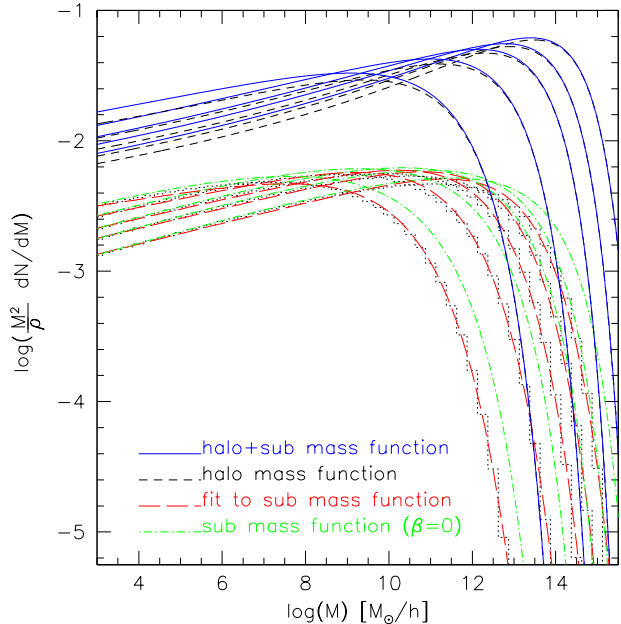


Figure 18. Number density per $M^2/\bar{\rho}$ of substructures (histograms) at redshifts $z = 0, 0.5, 1, 2, 4$ (top to bottom at massive end); dashed curves show the result of fitting to equation (10). For comparison, short-dashed curves show the host halo mass function (from Sheth & Tormen 1999) at the same redshifts. The solid line show the halo+substructure mass function and the dot-dashed the analytical solution for the global substructure mass function when $\beta \approx 0$ (eq. 12).

minimizing

$$\chi^2 = \sum_i \left[\log(y(m_{\text{sb}})) - \log \left(m_{\text{sb}} \frac{dn(m_{\text{sb}})}{d \ln m_{\text{sb}}} \right)_i \right]^2, \quad (11)$$

where the sum is over the various values of $\ln m_{\text{sb}}$ at which we computed the integral (the centers of the histograms shown in Figure 18). Table 2 lists the resulting best fit parameters. As can be seen from the last column of the Table, the shape is fit to an accuracy of about 2%. Solid curves in the figure show the halo+substructures mass function.

When $\beta \approx 0$, equation (9) becomes

$$\begin{aligned} \frac{dn(m_{\text{sb}})}{d \ln m_{\text{sb}}} &= N_{M_0} (1+z)^{1/2} (m_{\text{sb}})^{\alpha} \bar{\rho} \frac{A}{\sqrt{\pi}} \\ &\quad \times [0.812 \Gamma(0.2, 0.353\nu) + \Gamma(0.5, 0.353\nu)] \end{aligned} \quad (12)$$

where $A \approx 0.322$ is the normalization of the halo mass function and $\nu = \delta_c(z)^2/S(m)$. The dot-dashed curves in Figure 18 show this approximation. Clearly, neglecting the high-mass exponential cut off is not a good approximation.

7 SUMMARY AND CONCLUSION

We estimated the mass function of substructures by following all the branches (rather than just the main branch) of the merger history tree of a halo. This distribution, dN/dm_{sb} , depends on the mass of the host halo, when the halo was identified, and its formation time. However when the number of substructures per host halo mass is considered, the distribution turns to be “universal” at a given redshift, but

z	η	a_0	$\log(\bar{m}_0)$	γ	σ_{rms}
0	0.07930 ± 0.0002	7.812 ± 0.001	$13.10_{-0.06}^{-0.07}$	$0.407_{-0.005}^{+0.025}$	0.027
0.5	0.07631 ± 0.0002	7.944 ± 0.001	$12.61_{-0.06}^{-0.06}$	$0.386_{-0.005}^{+0.020}$	0.026
1	0.07308 ± 0.0002	8.032 ± 0.001	$12.13_{-0.05}^{-0.06}$	$0.366_{-0.012}^{+0.017}$	0.023
2	0.06720 ± 0.0003	8.142 ± 0.001	$11.29_{-0.05}^{-0.10}$	$0.336_{-0.012}^{+0.018}$	0.019
4	0.05222 ± 0.0003	8.267 ± 0.002	$10.06_{-0.03}^{-0.08}$	$0.309_{-0.008}^{+0.013}$	0.016

Table 2. Best fit parameter to the global substructure mass function at the five considered redshifts. The last column shows the rms scatter between the distribution and the best fit.

simulations with higher mass resolution are required to determine if this is true even when the host halo mass is smaller than $10^{11}h^{-1}M_{\odot}$. This universal shape is characterized by a power law of slope -0.9 at low masses, times an exponential cut-off when the substructure mass approaches that of the host halo. This distribution can be integrated to obtain the substructure virial mass fraction and the mean number of clumps at a given host halo mass.

At fixed host halo mass, the haloes which formed at higher redshift tend to have less substructure. In addition, more massive host haloes have more substructures than less massive ones. The first trend arises because satellites which spend more time in the potential well of their host lose a larger fraction of their initial mass (or can be totally disrupted). Massive haloes formed more recently, so this same mechanism explains the second trend. Similar trends are seen if we replace halo formation time (which is not observable) with the concentration parameter of the halo density profile (which is).

We also showed that the Poisson model, with a mean that depends on host halo mass, is a reasonable description of the substructure counts within a host halo. However, the second and third factorial moments of the substructure counts are ~ 5 percent larger than for a Poisson model with the same mean counts. As observations improve, this may become important in Halo Model parametrization of large scale structure which relate halo substructure to galaxies.

At fixed mass, the mean number of substructures above some minimum mass is larger at high redshift. Although this is not unexpected – the higher redshift haloes have had less time to destroy their substructures – we argued that the redshift dependence could be well-approximated by assuming that the anti-correlation between substructure abundance and host halo concentration we measure at $z = 0$ does not evolve. At fixed mass, higher redshift haloes are less concentrated – in effect, our assumption is that the same physics which affects the concentrations also affects the substructure. This allows us to provide a simple prescription for the redshift evolution of substructures, which we use to provide analytic approximations for the result of integrating the substructure mass function over all host halo masses. These results should find use in halo model interpretations of the (evolution of the) galaxy clustering signal in large scale sky surveys (e.g., [van den Bosch et al. 2007](#); [Wake et al. 2008](#)).

ACKNOWLEDGMENTS

CG thanks Robert Smith and Jorge Moreno for the hospitality and suggestions during his period spent in Philadelphia, and Matthias Bartelmann for useful discussion during the final writing of the paper. Gao Liang for providing us SUBFIND catalogues of the GIF2 simulation. RKS thanks R. Skibba and the members of the MPI-Astronomie, Heidelberg for their hospitality, and NSF-AST 0908241 for support. The authors thank also the referee for useful discussions and comments

REFERENCES

- Angulo, R. E., Lacey, C. G., Baugh, C. M., & Frenk, C. S. 2008, arXiv:0810.2177
- Benson, A. J., Lacey, C. G., Frenk, C. S., Baugh, C. M., & Cole, S. 2004, MNRAS, 351, 1215
- Bond, J. R., Cole, S., Efstathiou, G., & Kaiser, N. 1991, ApJ, 379, 440
- Bradač, M., Schneider, P., Lombardi, M., Steinmetz, M., Koopmans, L. V. E., & Navarro, J. F. 2004, Aap, 423, 797
- Bryan, G. L., & Norman, M. L. 1998, ApJ, 495, 80
- Bullock, J. S., Kolatt, T. S., Sigad, Y., Somerville, R. S., Kravtsov, A. V., Klypin, A. A., Primack, J. R., & Dekel, A. 2001, MNRAS, 321, 559
- Cooray, A., & Sheth, R. 2002, PhR, 372, 1
- Croton, D. J., et al. 2006, MNRAS, 365, 11
- Davis, M., Efstathiou, G., Frenk, C. S., & White, S. D. M. 1985, ApJ, 292, 371
- De Lucia, G., Kauffmann, G., Springel, V., White, S. D. M., Lanzoni, B., Stoehr, F., Tormen, G., & Yoshida, N. 2004, MNRAS, 348, 333
- De Lucia, G., & Blaizot, J. 2007, MNRAS, 375, 2
- Diemand, J., Kuhlen, M., & Madau, P. 2007, ApJ, 657, 262
- Madau, P., Diemand, J., & Kuhlen, M. 2008, ApJ, 679, 1260
- Dolag, K., Bartelmann, M., Perrotta, F., Baccigalupi, C., Moscardini, L., Meneghetti, M., & Tormen, G. 2004, A&A, 416, 853
- Eke, V. R., Cole, S., & Frenk, C. S. 1996, MNRAS, 282, 263
- Fornengo, N., Pieri, L., & Scopel, S. 2004, Physical Review D, 70, 103529
- Gao, L., White, S. D. M., Jenkins, A., Stoehr, F., & Springel, V. 2004, MNRAS, 355, 819

- Gao, L., Springel, V., & White, S. D. M. 2005, *MNRAS*, 363, L66
- Gao, L., & White, S. D. M. 2007, *MNRAS*, 377, L5
- Gao, L., Navarro, J. F., Cole, S., Frenk, C. S., White, S. D. M., Springel, V., Jenkins, A., & Neto, A. F. 2008, *MNRAS*, 387, 536
- Ghigna, S., Moore, B., Governato, F., Lake, G., Quinn, T., & Stadel, J. 2000, *ApJ*, 544, 616
- Gill, S. P. D., Knebe, A., & Gibson, B. K. 2004, *MNRAS*, 351, 399
- Gill, S. P. D., Knebe, A., Gibson, B. K., & Dopita, M. A. 2004, *MNRAS*, 351, 410
- Giocoli, C., Moreno, J., Sheth, R. K., & Tormen, G. 2007, *MNRAS*, 111
- Giocoli, C., Tormen, G., & van den Bosch, F. C. 2008, *MNRAS*, 386, 2135
- Giocoli, C., Pieri, L., & Tormen, G. 2008, *MNRAS*, 387, 689
- Giocoli, C., Pieri, L., Tormen, G., & Moreno, J. 2009, *MNRAS*, 395, 1620
- Harker, G., Cole, S., Helly, J., Frenk, C., & Jenkins, A. 2006, *MNRAS*, 367, 1039
- Hester, J. A., & Tasitsiomi, A. 2009, arXiv:0902.4489
- Ishiyama, T., Fukushige, T., & Makino, J. 2008, *PASJ*, 60, L13
- Ishiyama, T., Fukushige, T., & Makino, J. 2009, *ApJ*, 696, 2115
- Jenkins, A., Frenk, C. S., White, S. D. M., Colberg, J. M., Cole, S., Evrard, A. E., Couchman, H. M. P., & Yoshida, N. 2001, *MNRAS*, 321, 372
- Kamionkowski, M., & Liddle, A. R. 2000, *Physical Review Letters*, 84, 4525
- Kauffmann, G., Colberg, J. M., Diaferio, A., & White, S. D. M. 1999, *MNRAS*, 303, 188
- Kazantzidis, S., Bullock, J. S., Zentner, A. R., Kravtsov, A. V., & Moustakas, L. A. 2008, *ApJ*, 688, 254
- Kazantzidis, S., Zentner, A. R., Kravtsov, A. V., Bullock, J. S., & Debattista, V. P. 2009, *ApJ*, 700, 1896
- Knebe, A., Green, A., & Binney, J. 2001, *MNRAS*, 325, 845
- Koposov, S. E., Yoo, J., Rix, H.-W., Weinberg, D. H., Macciò, A. V., & Escudé, J. M. 2009, *ApJ*, 696, 2179
- Kravtsov, A. V., Gnedin, O. Y., & Klypin, A. A. 2004, *ApJ*, 609, 482
- Lacey, C., & Cole, S. 1993, *MNRAS*, 262, 627
- Li, Y., Mo, H. J., & Gao, L. 2008, *MNRAS*, 389, 1419
- Li, Y., & Mo, H. 2009, arXiv:0908.0301
- Macciò, A. V., & Miranda, M. 2006, *MNRAS*, 368, 599
- Macciò, A. V., Dutton, A. A., van den Bosch, F. C., Moore, B., Potter, D., & Stadel, J. 2007, *MNRAS*, 378, 55
- Macciò, A. V., Kang, X., & Moore, B. 2009, *ApJL*, 692, L109
- Meneghetti, M., Bartelmann, M., Jenkins, A., & Frenk, C. 2007, *MNRAS*, 381, 171
- Moore, B., Governato, F., Quinn, T., Stadel, J., & Lake, G. 1998, *ApJL*, 499, L5
- Moore, B., Ghigna, S., Governato, F., Lake, G., Quinn, T., Stadel, J., & Tozzi, P. 1999, *ApJ*, 524, L19
- Navarro, J. F., Frenk, C. S., & White, S. D. M. 1996, *ApJ*, 462, 563
- Navarro, J. F., Frenk, C. S., & White, S. D. M. 1997, *ApJ*, 490, 493
- Natarajan, P., De Lucia, G., & Springel, V. 2007, *MNRAS*, 376, 180
- Neto, A. F., et al. 2007, *MNRAS*, 381, 1450
- Peebles, P. J. E. 1980, Research supported by the National Science Foundation. Princeton, N.J., Princeton University Press, 1980. 435 p.,
- Pieri, L., Bertone, G., & Branchini, E. 2008, *MNRAS*, 384, 1627
- Press, W. H., & Schechter, P. 1974, *ApJ*, 187, 425
- Rasia, E., Tormen, G., & Moscardini, L. 2004, *MNRAS*, 351, 237
- Ricotti, M., & Gnedin, N. Y. 2005, *ApJ*, 629, 259
- Saro, A., De Lucia, G., Dolag, K., & Borgani, S. 2008, *MNRAS*, 391, 565
- Scoccimarro, R., Sheth, R. K., Hui, L., & Jain, B. 2001, *ApJ*, 546, 20
- Seljak, U., & Zaldarriaga, M. 1996, *ApJ*, 469, 437
- Shaw, L. D., Weller, J., Ostriker, J. P., & Bode, P. 2006, *ApJ*, 646, 815
- Shaw, L. D., Weller, J., Ostriker, J. P., & Bode, P. 2007, *ApJ*, 659, 1082
- Sheth, R. K. 1998, *MNRAS*, 300, 1057
- Sheth, R. K., Bernardi, M., Schechter P. L., et al. 2003, *ApJ*, 594, 225
- Sheth, R. K., & Diaferio, A. 2001, *MNRAS*, 322, 901
- Sheth, R. K., & Jain, B. 2003, *MNRAS*, 345, 529
- Sheth, R. K., & Tormen, G. 1999, *MNRAS*, 308, 119
- Sheth, R. K., Mo, H. J., & Tormen, G. 2001, *MNRAS*, 323, 1
- Sheth, R. K., & Tormen, G. 2002, *MNRAS*, 329, 61
- Sheth, R. K., & Tormen, G. 2004, *MNRAS*, 349, 1464
- Sheth, R. K., & Tormen, G. 2004, *MNRAS*, 350, 1385
- Simon, J. D., & Geha, M. 2007, *ApJ*, 670, 313
- Spergel, D. N., et al. 2003, *ApJS*, 148, 175
- Springel, V., White, S. D. M., Tormen, G., & Kauffmann, G. 2001, *MNRAS*, 328, 726
- Springel, V., et al. 2005, *Nat*, 435, 629
- Springel, V., et al. 2008, *MNRAS*, 391, 1685
- Springel, V., et al. 2008, *Nat*, 456, 73
- Stoehr, F. 1999, Diploma Thesis, at Physics Department Technische Universität München
- Stoehr, F., White, S. D. M., Springel, V., Tormen, G., & Yoshida, N. 2003, *MNRAS*, 345, 1313
- Susa, H., & Umemura, M. 2004, *ApJL*, 610, L5
- Tormen, G., Bouchet, F. R., & White, S. D. M. 1997, *MNRAS*, 286, 865
- Tormen, G., Diaferio, A., & Syer, D. 1998, *MNRAS*, 299, 728
- Tormen, G. 1998, *MNRAS*, 297, 648
- Tormen, G., Moscardini, L., & Yoshida, N. 2004, *MNRAS*, 350, 1397
- van den Bosch, F. C. 2002, *MNRAS*, 331, 98
- van den Bosch, F. C., Tormen, G., & Giocoli, C. 2005, *MNRAS*, 359, 1029
- van den Bosch, F. C., et al. 2007, *MNRAS*, 376, 841
- Yoshida, N., Sheth, R. K., & Diaferio, A. 2001, *MNRAS*, 328, 669
- Walker, M. G., Belokurov, V., Evans, N. W., Irwin, M. J., Mateo, M., Olszewski, E. W., & Gilmore, G. 2009, *ApJL*, 694, L144
- Wake D. A., et al., 2008, *MNRAS*, 387, 1045

- Wechsler, R. H., Bullock, J. S., Primack, J. R., Kravtsov, A. V., & Dekel, A. 2002, *ApJ*, 568, 52
- Weller, J., Ostriker, J. P., Bode, P., & Shaw, L. 2005, *MNRAS*, 364, 823
- Wetzel, A. R., Cohn, J. D., & White, M. 2009, *MNRAS*, 395, 1376
- Wetzel, A. R., Cohn, J. D., & White, M. 2009, *MNRAS*, 394, 2182
- White S. D. M., Rees M. J., 1978, *MNRAS*, 183, 341
- Zhao D. H., Jing Y. P., Mo H. J., Börner G., 2009, *ApJ*, submitted (arXiv:0811.0828)

APPENDIX A: COMPARISON WITH PREVIOUS WORK

Our new substructure algorithm is a modification of that in [Giocoli et al. \(2008a\)](#) and is rather different from that of [Gao et al. \(2004\)](#).

Our new algorithm returns smaller substructure mass fractions, especially at large host halo masses, than did our old one (i.e., that of [Giocoli et al. 2008a](#)); it is more conservative about identifying self-bound structures. This is shown in [Figure A1](#), where the change at the high mass end is more than 50%. It is smaller at the low mass end, where the host halo masses are approaching that of the mass resolution of the subhaloes. This shows explicitly that if one wants to think of our new algorithm as taking the subhaloes of [Giocoli et al. \(2008a\)](#) and partitioning them up into smaller substructures, then some of the subhalo mass from the old algorithm is now assigned to the host halo rather than to substructures. The new value of the substructure mass fraction for the most massive haloes agrees pretty well with other algorithms, that give values around 10% of the host halo mass¹ ([Springel et al. 2001](#); [Weller et al. 2005](#)).

The changes in mass fraction between the two algorithms shown in [Figure A1](#) can be understood also considering the fact that when we split a subhalo in pieces (sub-subhaloes), we must also recompute the centre-of-velocity (from which we compute the kinetic energy) and, more importantly, we calculate the new potential energy only using the new subsets of particles. This forces the new potential energy to be less negative than before (i.e. the same particle is assigned a less negative potential energy than before, because the potential wells are shallower), and so many particles which reside in-between the density peaks of the various sub-subhaloes, even if they were bound to the subhalo as a whole, happen to be unbound to any of the sub-subhaloes, and often are unbound to the main subhalo itself. This is because the splitting removed all the secondary density peaks, so the global potential well becomes shallower decreasing the self-bound mass of the clumps.

[Figure A2](#) compares the substructure mass functions found by our algorithm, that of [Gao et al. \(2004\)](#), and the subhalo mass function of [Giocoli et al. \(2008a\)](#). To facilitate comparison with [Gao et al. \(2004\)](#), we have chosen to use the same mass bins and host halo definition as [Gao et al.](#)

¹ Comparing our new algorithm with the result of SUBFIND for the most massive halo at $z = 0$ we found respectively 6.5% and 6.2% of $M_{200,c}$ to be in substructures.

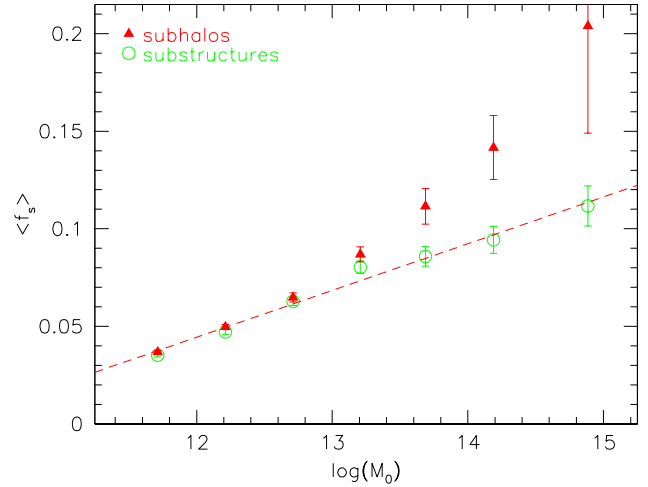


Figure A1. Mass fraction in the subhaloes of [Giocoli et al. \(2008a\)](#) and in substructures found by our new algorithm (filled and open symbols, respectively).

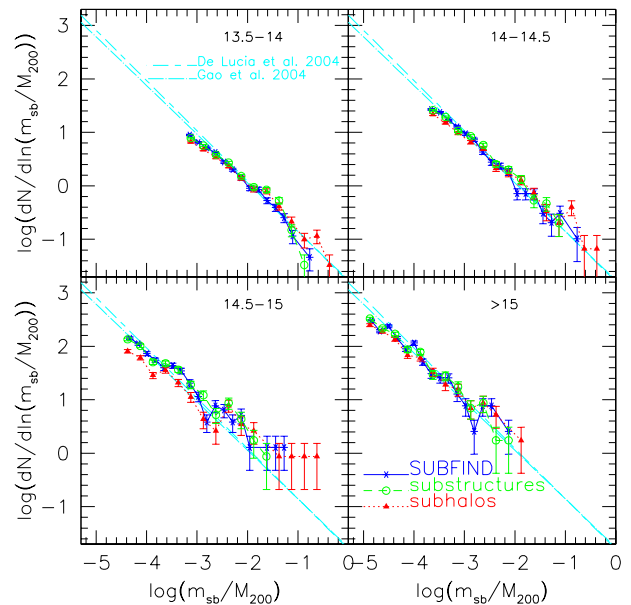


Figure A2. Comparison of substructure mass functions, expressed as a function of m_{sb}/M_{200} found by our algorithm, that of [Gao et al. \(2004\)](#) (SUBFIND), and the subhaloes⁽¹⁾ of [Giocoli et al. \(2008a\)](#).

(2004); i.e., host haloes are 200 times the critical density. We will use M_{200} to distinguish this definition from M_{vir} , the quantity used in the main text. Note that $M_{200} < M_{vir}$, with the difference increasing at late times (lower redshifts). Our new algorithm (open symbols) takes the subhaloes returned by our old algorithm (triangles) and partitions them up into smaller pieces; it removes objects from large $m_{sb} \sim M_{200}$ and adds objects to $m_{sb} \ll M_{200}$. The resulting distribution is indeed very similar to that found by [Gao et al. \(2004\)](#) using SUBFIND (crosses). The dashed and the dot-dashed lines show the fit-by-eye of the cluster size halo by [De Lucia et al. \(2004\)](#) and [Gao et al. \(2004\)](#).

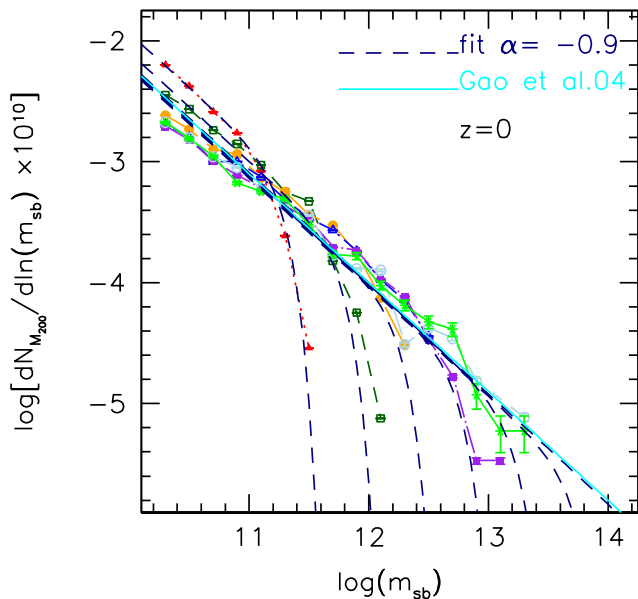


Figure A3. Substructure mass functions found by our algorithm when host haloes are defined to be 200 times the critical density. This is the analog of Figure 4 in the main text. Solid line show equation (1) by Gao et al. (2004).

Figure A2, which shows $dN/d\ln(m_{sb}/M_{200})$, is the analog of Figure 3 in the main text. However, in our discussion of $(dN/d\ln m_{sb})/M_{vir}$ in the main text, we found that the normalization of our substructure mass function appeared to be larger than that reported by Gao et al. (2004), and we argued that this could be attributed to the difference in how we define host halo masses. Since the definitions are the same here, Figure A3 shows $(dN/d\ln m_{sb})/M_{200}$, which is the analog of Figure 4. Note that the normalization is indeed lower for M_{200} than it is for M_{vir} .

In addition, we argued in the main text that because $M_{200} < M_{vir}$, the host halo formation times for haloes of a given M_{200} should be higher than those for haloes that have the same numerical value for M_{vir} . Figure A4 shows that this is indeed the case. As a result, we generically expect M_{200} haloes at the present time to have less substructure than haloes with the same numerical value of M_{vir} (for comparison see Figure 4).

APPENDIX B: RESCALING MASS DEFINITIONS

In the spherical collapse model, the density within the virial radius R_{vir} is assumed to be $\Delta_{vir}(z)$ times the critical density at the time of virialization, where Δ_{vir} is given by equation (1). In principle, this can be used as a criterion to identify bound objects. However, because the details involved in approximating the timescale to virialization are not well understood, this density is not the only one which has been used to identify haloes in simulations. For example Diemand et al. (2007) and related papers, and Dolag et al. (2004), define haloes as being 200 times the mean background density. The corresponding radius, $R_{200,b}$, is larger than R_{vir} at $z = 0$. On the other hand, Springel et al. (2001); Gao et

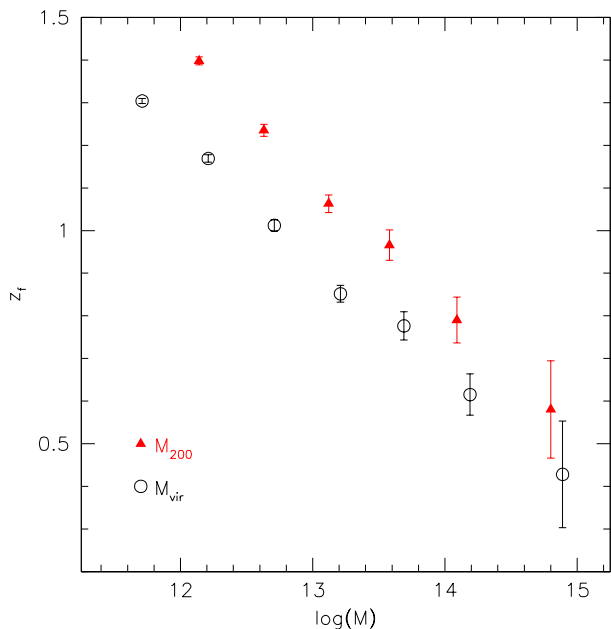


Figure A4. Dependence of formation time on definition of halo mass: haloes defined to be $200\rho_{crit}(z)$ will have formed at higher redshifts with respect to objects which are $\Delta_{vir}(z) < 200$ times the critical density. Note, here M corresponds to M_{200} in the case of the solid triangles and to M_{vir} in the case of the open circles.

al. (2004); Springel et al. (2005) and related papers define haloes as having average densities 200 times the critical density. The corresponding radius $R_{200,c}$ is smaller than R_{vir} at $z = 0$. Note that all three definitions become comparable at high redshift.

For each definition, the enclosed mass can be read as:

$$M_i = \frac{4\pi}{3} R_i^3 \Delta_i(z) \rho_c, \quad (\text{B1})$$

where $i = \{(vir), (200, b), (200, c)\}$.

To rescale the different mass definitions we estimate $R_{200,b}/R_{vir}$ and $R_{200,c}/R_{vir}$ at various z by computing $R_{200,c}$ and $R_{200,b}$ from the density profile of our selected haloes (which were defined to have sizes R_{vir}). We consider 8 simulation outputs between $z = 0$ and $z = 3$. Figure B1 shows the evolution of the ratio $R_{200,b}/R_{vir}$. The filled pentagons show the mean value of this ratio when averaged over haloes of all masses; the other data points are for different mass bins, here expressed as $\nu = \delta_c^2(z)/S(M)$. The error bars show the rms scatter of the distribution at each z for each halo sample. The solid curve corresponds to:

$$\frac{R_{200,b}}{R_{vir}} = 1.236 \left[\frac{\Delta_{vir}(z)}{\Delta_{vir}(0)} \right]^{-0.438}. \quad (\text{B2})$$

where $\Delta_{vir}(z)$ is given by equation (1) in the main text. The rms scatter between this curve and the measured points is $\sigma_{rms} = 1.1\%$.

Figure B2 shows the evolution of the ratio $R_{200,c}/R_{vir}$. Data points and error bars are like in Figure B1. The solid curve corresponds to:

$$\frac{R_{200,c}}{R_{vir}} = 0.746 \left[\frac{\Delta_{vir}(z)}{\Delta_{vir}(0)} \right]^{0.395}, \quad (\text{B3})$$

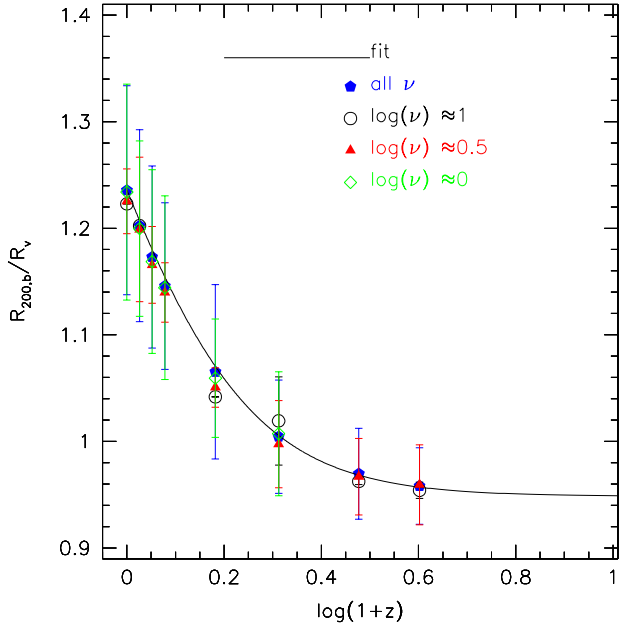


Figure B1. Evolution of the ratio $R_{200,b}/R_{\text{vir}}$. Symbols show the simulation data for different masses (here expressed as ν); solid curve shows equation (B2).

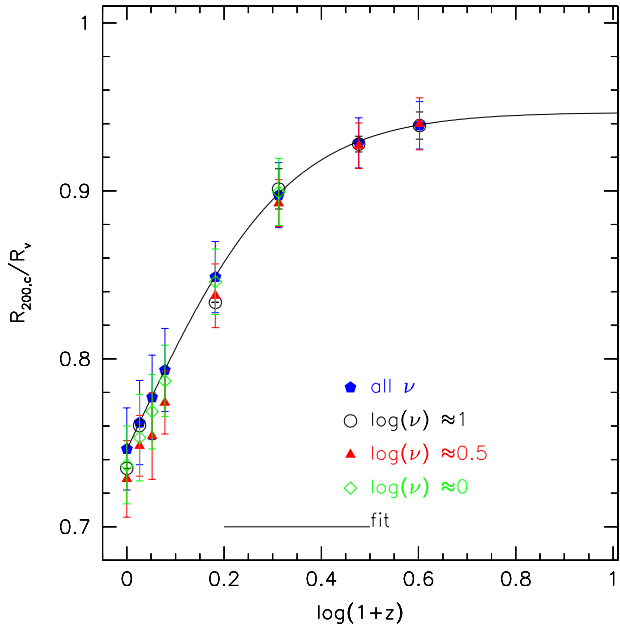


Figure B2. Evolution of the ratio $R_{200,c}/R_{\text{vir}}$. Symbols are as in Figure B1; solid curve shows equation (B3).

that well fit the mean value computed considering all haloes, with a $\sigma_{rms} = 0.08\%$.

For consistency we check that the ratio $R_{200,b}/R_{200,c}$ approach to unity at high redshift where the universe is matter dominated and the dark matter density approaches the critical one.

Equations (B2) and (B3) are also useful for rescaling different definitions of halo concentration. Halo density profiles are well fit by the functional form of Navarro et al.

(1997); this form has a characteristic scale r_s , where the density profile changes slope, and the concentration is defined as the ratio of this scale to the virial radius. Thus, depending on the density used to define the halo, one might have $c_{200} = R_{200,c}/r_s$ (Navarro et al. 1997; Neto et al. 2007; Gao et al. 2008), $c_{200,b} = R_{200,b}/r_s$ (Dolag et al. 2004) or $c_{\text{vir}} = R_{\text{vir}}/r_s$ (Bullock et al. 2001). Because r_s itself is a physical quantity that does not depend on the halo mass definition, the expressions above can be used to transform between the different definitions of concentration.